Title
Ultrafast terahertz electrodynamics of cuprate superconductors

Author
Cremin, Kevin Alan

Publication Date
2019

UNIVERSITY OF CALIFORNIA SAN DIEGO

Ultrafast terahertz electrodynamics of cuprate superconductors

A dissertation submitted in partial satisfaction of the
requirements for the degree
Doctor of Philosophy

in

Physics

by

Kevin Cremin

Committee in charge:

Professor Richard Averitt, Chair
Professor Michael Fogler
Professor Joseph Ford
Professor Vitaliy Lomakin
Professor Oleg Shpyrko

2019

The dissertation of Kevin Cremin is approved, and it is acceptable in quality and form for publication on microfilm and electronically:

Chair

University of California San Diego

2019

DEDICATION

To my parents who have given unconditional love and support every step of the way.

TABLE OF CONTENTS

LIST OF FIGURES

ACKNOWLEDGEMENTS

The journey along this PhD for me has been monumental period of growth as a scientist and as a person. Working through the many challenges and setbacks have taught me that patience and perseverance are the key qualities needed to overcome any obstacle, and the breakthroughs and triumphs that follow are sweeter than one could have imagined.

First, I would like to thank my advisor, Richard Averitt, for taking me into his group and giving me the opportunity to help develop the experimentation in the lab. He has showed continual support throughout all the experimental setbacks and has given me space to develop and try my own ideas.

I would also like to thank Jingdi for teaching me the experimental skills and patience required to build and operate optical measurements. He has been an unparalleled source of wisdom for myself during the majority of my PhD and has always offered help and insight for any kind of problem.

I am very thankful to have shared the laboratory space with the other members of the Averitt lab. Not only have we helped each other each step of they, but have developed friendships that will continue far past our time together at UCSD. I would especially like to thank the four other graduate students I have spent the most time with: Peter, Gufeng, Dylan and Jacob. We all started with an empty laboratory and limited knowledge of optics, but have managed to build a state of the art optics lab together. The camaraderie we have developed as a group has made working and spending time in the lab a joy and something to look forward to.

In every chapter of my life, my parents have showed unconditional support and encouragement to follow the pursuit of knowledge. I would like to thank them for continually sending their love and reassurance that everything will be okay.

Finally, I would like to thank my girlfriend Talita for helping me get through the thesis writing process.

Chapter 4 is in part a reprint of work published in *Proceedings of the National Academy*

of Sciences **116**, 40 (2019), 1987519879 [14]. Kevin A. Cremin, Jingdi Zhang, Christopher C. Homes, G. D. Gu, Zhiyuan Sun, Michael M. Fogler, Andrew J. Millis, D. N. Basov, and Richard D. Averitt. The thesis auther was the primary author of this chapter.

Chapter 5 is a discussion of recent preliminary results. The research has been possible with contributions from Kevin Cremin, Kelson Kaj, Ian Hammock, Jacob Schalch, Chunxu Chen, Xiaguan Zhao, Dimitri Basov, Xin Zhang, and Richard Averitt. The thesis author was the author of this chapter.

VITA

2013	B.S. in Physics *cum laude*, University of California, Santa Cruz
2013-2014	Graduate Teaching Assistant, University of California, San Diego
2015	M.S in Physics, University of California, San Diego
2019	Ph.D. in Physics, University of California, San Diego

PUBLICATIONS

Kevin Cremin, Jingdi Zhang, Christopher C. Homes, G. D. Gu, Zhiyuan Sun, Michael Fogler, Andrew J. Millis, D. N. Basov, and Richard D. Averitt. *Photo-enhanced metastable c-axis electrodynamics in stripe oredered cuprate* $La_{1.885}Ba_{0.115}CuO_4$” Proceedings of the National Academy of Sciences **116**, (40) 19875-19879 (2019).

Yakun Yuan, Peter Kissin, Danilo Puggioni, **Kevin Cremin**, Shiming Lei, Yu Wang, Zhiqiang Mao, James M. Rondinelli, Richard Averitt, and Venkatraman Gopalan. ”*Ultrafast quasiparticle dynamics in the correlated semimetal* $Ca_3Ru_2O_7$” Phys. Rev. B **99**, 155111 (2019).

Xiaoguang Zhao, Yu Wang, Jacob Schalch, Guangwu Duan, **Kevin Cremin**, Jingdi Zhang, Chunxu Chen, Richard D. Averitt, and Xin Zhang. ”*Optically Modulated Ultra-Broadband All-Silicon Metamaterial Terahertz Absorbers*” ACS Photonics **6**, 830-837 (2019).

Meng Wu, Xiaoguang Zhao, Jingdi Zhang, Jacob Schalch, Guangwu Duan, **Kevin Cremin**, Richard D. Averitt, and Xin Zhang. ”*A thre-dimensional all-metal terahertz metamaterial perfect absorber*” Appl. Phys. Lett. **111** 051101 (2017).

ABSTRACT OF THE DISSERTATION

Ultrafast terahertz electrodynamics of cuprate superconductors

by

Kevin Cremin

Doctor of Philosophy in Physics

University of California San Diego, 2019

Professor Richard Averitt, Chair

Since the discovery of superconductivity, the potential applications of superconductors has pushed the research of these materials into the forefront of physics. With the current rate of technological developments, the discovery of room temperature superconductors seems only steps away. The use of light, i.e. spectroscopy, has been one of the greatest tools used in modern physics for furthering our understanding of material properties. Not only can we use light to probe the underlying physics, but we can also use light to manipulate and control a materials properties by design. In this thesis, I will present two different projects I have worked on involving high-T_c superconductors and using light excitation to induce a metastable phase transition and probe the materials nonlinear response. The first three chapters cover a brief background of superconductors and recent advances in light-induced superconductivity, experimental techniques built and developed by myself, and the method of analysis. The first research endeavour I report on is photo-excitation of the highly charge-ordered cuprate $La_{2-x}Ba_xCuO_4$. After excitation we are able to partially melt the competing charge-order and observe a long-lived metastable state which shows signatures of superconducting behaviour above T_c. The second research project explores the nonlinear *c*-axis response of $La_{2-x}Sr_xCuO_4$ using high field THz spectroscopy and we observe third harmonic generation by driving the Josephson plasma resonance. A metamaterial is also applied to the crystals surface and we observe pronounced nonlinear effects above and below T_C not present for linear field strengths.

Chapter 1

Superconductivity

1.1 High-T_C Cuprates

High temperature superconduncting cuprates were discovered in 1986[6], and with that came a new found enthusiasm for the condensed-matter community. Before this, the highest T_c was only 23 K and Bardeen-Cooper-Schrieffer (BCS) theory predicted the upper limit on superconductivity to be $\sim$30-40 K, as above this temperature thermal fluctations would be comparable to the phonon-electron interaction energy. Surprisingly, the record T_c was broken by a ceramic mott insulator type of material, making it clear that some novel mechanism is a the foundation of this quantum state.

The $La_{2-x}CuO_4$ parent compound of many superconductors is a mott insulator which exhibits antiferromagnetic ordering at low temperatures. A Mott insulator differs fundamentally from a band insulator in the mechanism that limits the conductivity. Conduction in a band insulator is blocked by the Pauli exclusion principle, where the highest filled band contains two electrons per unit cell, no transfer of charge is allowed since all the orbitals are filled. A Mott insulator's conductivity is limited by electron-electron repulsion even when band theory would predict the material to be metallic. By doping the parent compound with elements containing one fewer electron (hole doping), conductivity is restored by creating free orbitals electrons jump to avoiding an increase in Coulomb repulsion energy[46]. Upon hole doping is also where these materials exhibit superconductivity, of which there is typically an optimal doping enabling a maximum T_c. The electronic properties of these materials are also two-dimensional since the doped charges reside in plane, with minimal coupling between planes. The two-dimensional superconducting layers are a typical characteristic of the high-T_c cuprates and lead to interesting electrodynamics along the insulating *c*-axis which are described in the next section.

In the past few decades it has become clear that spin and charge ordering occur in these materials at low temperatures[73, 35]. The onset of these collective modes often arise at the same or similar temperatures as superconductivity, believed to be a competing order reducing T_c. Although several studies have shown superconducting fluctuations within the charge/spin ordered states[2, 60, 47, 22]. Understanding the puzzling connection between superconductivity and these low temperature ordered states may be the missing piece in controlling the temperature at which superconductivity can exist.

1.2 Josephson Plasma Resonance

Along with superconductor's defining features of zero resistivity and expulsion of magnetic field below T_c, there is a another important property that was discovered by B.D. Josephson [38] in 1962 now known as the Josephson effect. When two superconducting materials are placed near each other(¡10 nm) with an insulating barrier in between as depicted in Fig. 1.1, there still exists probability of the superconducting cooper pairs to tunnel across the barrier, thus creating a superconducting current through an insulating region where a normal current would not exist. Josephson analyzed this situation and discovered the resulting phenomena that occur with this type of configuration.

In order to analyze a Josephson junction, let us consider the quantum mechanical wave

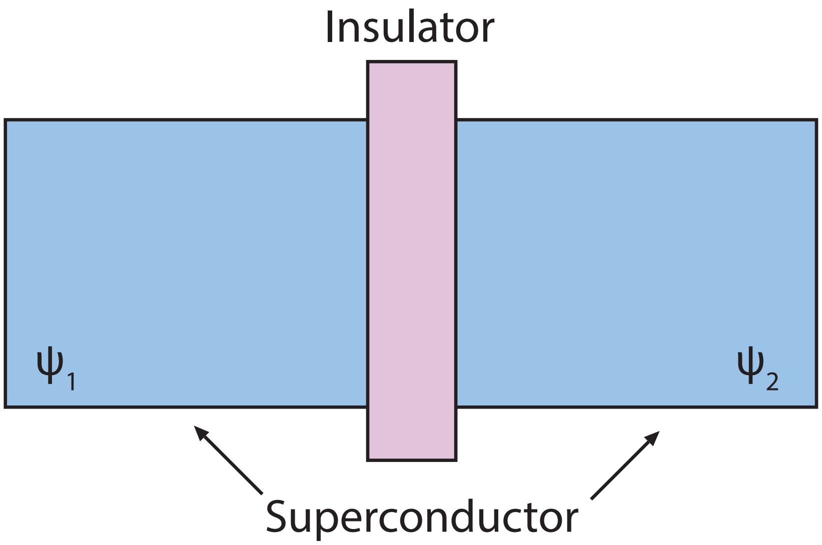

Figure 1.1: Two superconductors separated by a thin insulating barrier, containing wavefunctions ψ_1 and ψ_2.

functions ψ_1 and ψ_2 of the cooper pairs on each side of the barrier. The dynamics of each wave function can be determined by the following coupled Schrodinger equations[23]:

$$\begin{aligned} i\hbar\frac{\partial\psi_1}{\partial t} &= U_1\psi_1 + K\psi_2, \\ i\hbar\frac{\partial\psi_2}{\partial t} &= U_2\psi_2 + K\psi_1, \end{aligned} \tag{1.1}$$

where K is a constant representing the coupling strength across the barrier. If K were zero, equations 1.1 would just describe the lowest energy sate with energy U for each superconductor. If the two sides of the insulator are of the same material, we can create an energy difference by applying a voltage V across the junction resulting in $U_1 - U_2 = 2eV$ where e is the electron charge. For simplicity we define the zero of the energy to be halfway between which leads to

$$
\begin{aligned}
i\hbar\frac{\partial\psi_1}{\partial t} &= eV\psi_1 + K\psi_2, \\
i\hbar\frac{\partial\psi_2}{\partial t} &= -eV\psi_2 + K\psi_1,
\end{aligned}
\tag{1.2}
$$

which are the standard equations describing a system of two quantum mechanical states coupled together. We assume ψ_1 and ψ_2 have solutions of the form

$$
\begin{aligned}
\psi_1 &= \sqrt{\rho_0}e^{i\theta_1}, \\
\psi_2 &= \sqrt{\rho_0}e^{i\theta_2},
\end{aligned}
\tag{1.3}
$$

where ρ_0 is the superfluid density of electrons and θ_1 and θ_2 are the phases of the two opposite superconducting mediums. By substituting the equations for ψ_1 and ψ_2 into the coupled equations 1.2, and equating the real and imaginary parts we end up with four different equations

$$
\begin{aligned}
\frac{\partial\rho_1}{\partial t} &= +\frac{2}{\hbar}K\sqrt{\rho_1\rho_2}\sin\phi, \\
\frac{\partial\rho_2}{\partial t} &= -\frac{2}{\hbar}K\sqrt{\rho_1\rho_2}\sin\phi,
\end{aligned}
\tag{1.4}
$$

$$
\frac{\partial\phi}{\partial t} = \frac{2eV}{\hbar}, \tag{1.5}
$$

where $\phi = \theta_1 - \theta_2$ is the difference in phase between the two sides.

From the first two equations we can say that there is a flow of superconducting charge carriers from one side of the barrier to the other resulting in a current. In practice the superconducting density of either side is not actually changing, and this can be made sense of if we consider how we apply a voltage bias V. In this simple case, lets say the two superconducting sides are connected to the positive and negative terminals of a battery, any transfer of charge will be replenished on either side by the battery resulting in no net change in superfuild density. These equations describe how the densities would start to change under a potential difference, but still accurately tell the kind of current that would begin to flow. In a real scenario, ρ_1 and ρ_2 would both remain constant and equal to ρ_0 and we can write the current I across the insulating barrier as

$$I = I_0 \sin\phi \tag{1.6}$$

where $I_0 = 2K\rho_0/\hbar$. Equations 1.5 and 1.6 represent the main results from the general theory of the Josephson junction.

If we apply a DC voltage V_0 across the junction, we get a oscillating current of the form $I(t) = I_0 \sin(2eV_0 t/\hbar)$. Interestingly, by applying a DC voltage we can drive a current at frequency $f = 2eV_0/\hbar$. Since many cuprate superconductors are layered materials consisting of stacks of weakly coupled 2D superconducting planes(separation of $\sim$1 nm), they essentially form an array of small intrinsic Josephson junctions along the insulating direction(c-axis). By applying a voltage along the c-axis, one can initiate emission from the oscillating current at GHz or THz frequencies[4, 56, 40, 9], which can be used as a source for THz spectroscopy.

Now we consider the consequence of applying an oscillating voltage bias across the junction. This can be achieved with an incident plane wave electric field $E(t) = E_0 \cos(\omega t)$ oscillating at frequency ω. The system of stacked Josephson junctions behaves analogous to an RLC circuit with capacitance C and inductance L determined by the interlayer spacing and superfluid density. The plasma frequency of the oscillating superconducting charges is given by [61]

$$\omega_J = \left(\frac{8\pi e d I_0}{\hbar \varepsilon} \right)^{1/2} \tag{1.7}$$

where d is the interlayer spacing and ε is the permittivity. This has become a key feature of the high-T_c superconductors identified with spectroscopy also known as the Josephson plasma

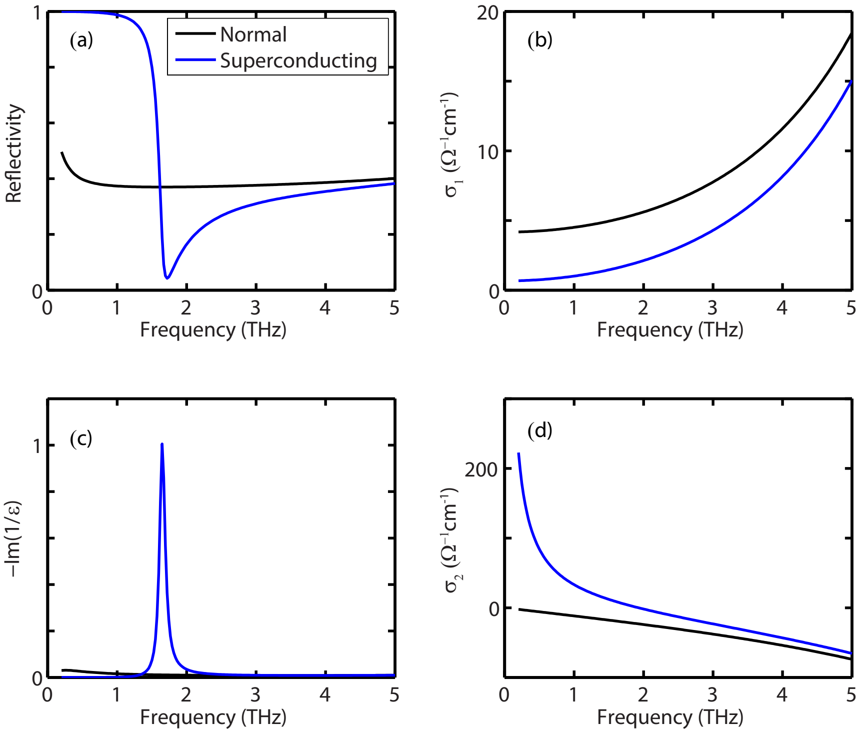

Figure 1.2: Key spectroscopic features of the *c*-axis Josephson plasma resonance measured in high-T_c superconductors. Panel (a) shows the *c*-axis reflectivity, panel (b) and (d) show the real and imaginary part of the optical conductivity and (c) the loss function. The normal insulating properties above T_c are plotted in black and the superconducting properties below T_c are plotted in blue.

resonance. Conveniently, the c-axis plasma frequency for most high-T_c superconductors lies within the 0.1-5 THz frequencies serving as a reporter of superconductor strength in Fourier-transform infrared and THz time domain spectroscopy. The key spectroscopic signatures of the Josephson plasma resonance are plotted in Fig. 1.2. Below T_c a plasma edge is observed in the c-axis reflectivity as well as peak in the loss function which is the imaginary part of $-1/\varepsilon$. Upon the superconducting transition, we see a decrease in the real part of the conductivity, as spectral weight at finite frequency is transferred to $\omega = 0$. Unlike in a typical BCS superconductor, there exists spectral weight below twice the superconducting gap 2Δ, due to a remaining existence of normal charge carriers. Superconductors, by nature have a scattering rate of 0 Hz, which mathematically is represented by a delta-function at $\omega = 0$ and this is seen as a $1/\omega$ divergence in the imaginary part of the conductivity.

1.3 Light induced superconductivity

Since the discovery of superconducting mercury in 1911, many advances have been made in the world of superconductivity. A main motivation in the research has been to increase the transition temperature where this phenomena begins to occur, and one day hopefully achieving a superconductor near room temperature. These scientific achievements come along with the development of theoretical understanding and new materials. The superconducting properties of material can be altered through doping, applying pressure or a magnetic field as well as using light. Intense laser pulses are frequently used to perturb materials, observing their relaxation pathways as well as inducing non-equilibrium properties not found otherwise. These techniques investigating light-matter interaction have been applied to superconductors over the past several decades and have helped to expand our understanding.

The current state of laser science has allowed for the generation of intense pulses of light from visible to mid-infrared and THz frequencies which can be tuned to effectively control cooperative physics at low temperatures. One of the first demonstrations of light-induced superconductivty was shown by D. Fausti *et. al.* in a striped-ordered cuprate $La_{1.675}Eu_{0.2}Sr_{0.125}CuO_4$[21]. Upon doping with Eu the material at low temperatures undergoes a tetragonal lattice distortion and exhibits spin and charge ordering which strongly reduces the superconducting transition Tc. Within the competition between phases of ordered charges and superconductivity lies a complex but interesting problem of how these materials become superconducting or not. By pumping the stripe-ordered system(non superconducting) at 10 K with 15 μm light, they resonantly drive an in-plane Cu-O stretching mode and observe the emergence of the *C*-axis Josephson plasma resonance in reflectivity with the use of THz time domain spectroscopy. The Josephson plasma resonance would suggest the interlayer coupling of newly formed superconducting planes. By strongly driving the lattice, the materials energy landscape can be perturbed enough to allow the system to settle into alternate ground states.

Enhanced superconductivity has also been measured in other cuprates with the use of light excitation. Enhanced interlayer tunneling has been observed in the bilayer cuprate $YBa_2Cu_3O_{6.5}$ after photo-excitation with 15 μm pump pulses[34] as well as the theoretical understanding[54]. In this system the interlayer separation is not equivalent and varies every other plane leading to two different coupling frequencies. The observation is described by a redistribution of spectral weight from the higher frequency Josephson plasma mode to the lower Josephson plasma mode. Rapid melting of the charge order in $La_{2-x}Ba_xCuO_4$ with intense near-infrared excitation has lead to transiently enhanced superconducting properties above and below T_c[52, 10] as seen from an emergence of a blue-shifted Josephson plasma edge. X-ray studies of LBCO have measured a weakening of the charge order after photo-excitation on a similar time-scale as the previous reports, thus supporting the claim of the mechanism of photo-induced superconductivity[41, 51].

While the fundamental pairing mechanism in the high-T_c cuprates is not well understood, it is evident that superconductivity occurs alongside with several other collective modes and lattice distortions. Whether beneficial or repressive to T_c, using light as a means to control these competitive ground states offers a promising pathway to furthering our understanding developing materials with even higher T_c

Chapter 2

Experimental Techniques

2.1 THz time domain spectroscopy

The use of THz spectroscopy has opened many doors in condensed matter physics allowing for the resolution of low frequency electrodynamics otherwise out of reach by other measurement techniques such as Fourier-transform infrared spectroscopy (FTIR)[5, 79]. Recent advances in Ultrafast THz pulses has allowed for the temporal evolution of carrier dynamics at the femtosecond time scale. This section provides an overview various methods for generating and detecting freely propagating broadband THz pulses used in the experiments of this thesis.

The basic idea of THz time-domain spectroscopy is to use a near-infrared femtosecond pulse to generate a single or multi-cycle THz pulse which is then detected with with the use of another near-infrared pulse through optical rectification described in this section. The temporal electric field can then be Fourier transformed in order to obtain the frequency resolved spectrum of the THz pulse. Two techniques of generating low intensity THz pulses used in the work of this thesis are by use of a commercial photoconductive antenna and difference frequency generation in ZnTe.

2.1.1 Photoconductive antenna

The photoconducitve antenna used was a large aperture TERA-SED$^{\text{TM}}$from Laser Quantum. The device contains interdigitated gold electrodes on the surface of a GaAs substrate which has a band gap of 1.4 eV. Incident ultrafast near-infrared pulses of 1.55 eV excite carriers into the conduction band which causes a rapid increase in the substrate conductivity and the excited charges are accelerated across the voltage bias provided by the electrodes. This sudden change in current dI/dt, occurring over a picosecond timescale, produces far field radiation in the THz frequencies ideal for spectroscopy[16]. From Larmor's formula we can see that the power P radiated from an accelerated amount of charge is given by[36]

$$P = \frac{2q^2}{3c^3}\left(\frac{dI}{dt}\right)^2 \tag{2.1}$$

where the q is the total charge excited into the conduction band of GaAs and c is the speed of light.

A schematic of the accelerated electrons producing far field THz radiation is displayed in figure 2.1(a), while panels (b) and (c) contain a measured THz pulse in the time domain and its Fourier transform respectively. The bandwidth of a generated THz pulse can be adjusted for the experimental desires by tuning the bias voltage and incident laser fluence [69, 19]. The THz pulse in fig. 2.1(b) was tuned to achieve a high amount of spectral content below 1 THz in order to observe the low frequency JPR around 200 GHz in $La_{1.885}Ba_{0.115}CuO_4$ as described in chapter 4.

2.1.2 Optical rectification

Another source of THz radiation implemented in our lab is generated via nonlinear optical processes in crystalline solids. Optical rectification and the Pockel's effect become apparent when considering a materials nonlinear interaction with strong electric fields. The polarizability P of a material is given by the relation

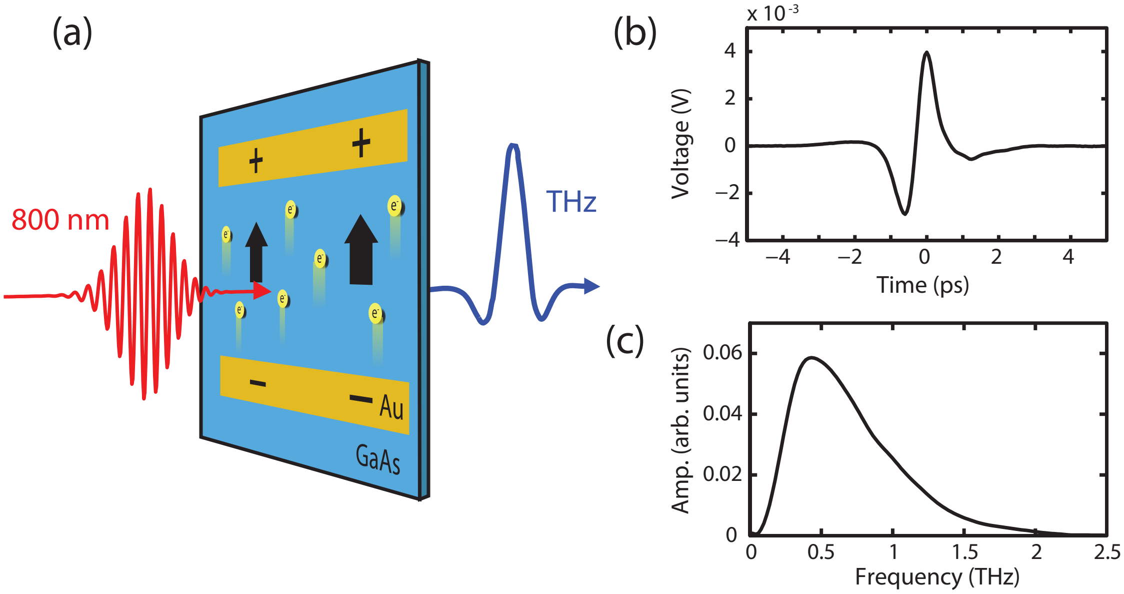

Figure 2.1: THz pulse generation from a photoconductive antenna. (a)Schematic of a near-infrared pulse exciting electrons into the conduction band of GaAs which are then accelerated across a voltage potential provided by two gold electrodes. The accelerated electrons emit far field radiation at THz frequencies through the back of the GaAs substrate. The temporal profile of the electric field (b) obtained from electro-optic sampling is plotted as well as the Fourier transform (c).

$$P = \chi(E)E, \tag{2.2}$$

where E is the applied electric field and χ is susceptibility. The polarization of a given material is proportional to the electric field. In order to understand the nonlinear interactions we can expand χ in powers of E giving[76]

$$P = \chi_1 E + \chi_2 E^2 + \chi_3 E^3 + \dots \tag{2.3}$$

The terms contributing to THz generation arise from the second order interactions of the expansion denoted as $P_2 = \chi_2 E^2$. Here the polarization depends on the square of the applied electric field or the product of two temporally overlapping fields. Let us consider two optical fields $E_1 = E_0 \cos(\omega_1 t)$ and $E_2 = E_0 \cos(\omega_2 t)$ oscillating at frequencies ω_1 and ω_2. Plugging the terms into equation for P_2 we arrive at

$$P_2 = \chi_2 E_1 E_2 = \frac{\chi_2 E_0^2}{2}\left[\cos\Big((\omega_1 + \omega_2)t\Big) + \cos\Big((\omega_1 - \omega_2)t\Big)\right]. \tag{2.4}$$

Here the the leading order nonlinear term P_2 is dependent on the strength of the second order susceptibility χ_2 and we can see that the polarization now also oscillates at two new frequencies denoted as the difference frequency $(\omega_1 - \omega_2)$ and sum frequency $(\omega_1 + \omega_2)$. The degenerate case where $\omega_1 = \omega_2$ describes second harmonic generation, but this term does not contribute to THz generation.

The difference frequency component is responsible for far-infrared THz generation when mixing two near-infrared photons of slightly different energy. Fortunately, ultrafast femtosecond near-infrared pulses intrinsically have a bandwidth $\Delta\omega$ where all the different frequencies within the pulse mix together to create a broadband THz specrtum. We consider a near-infrared Gaussian pulse in the time domain to have an electric field profile of the formd

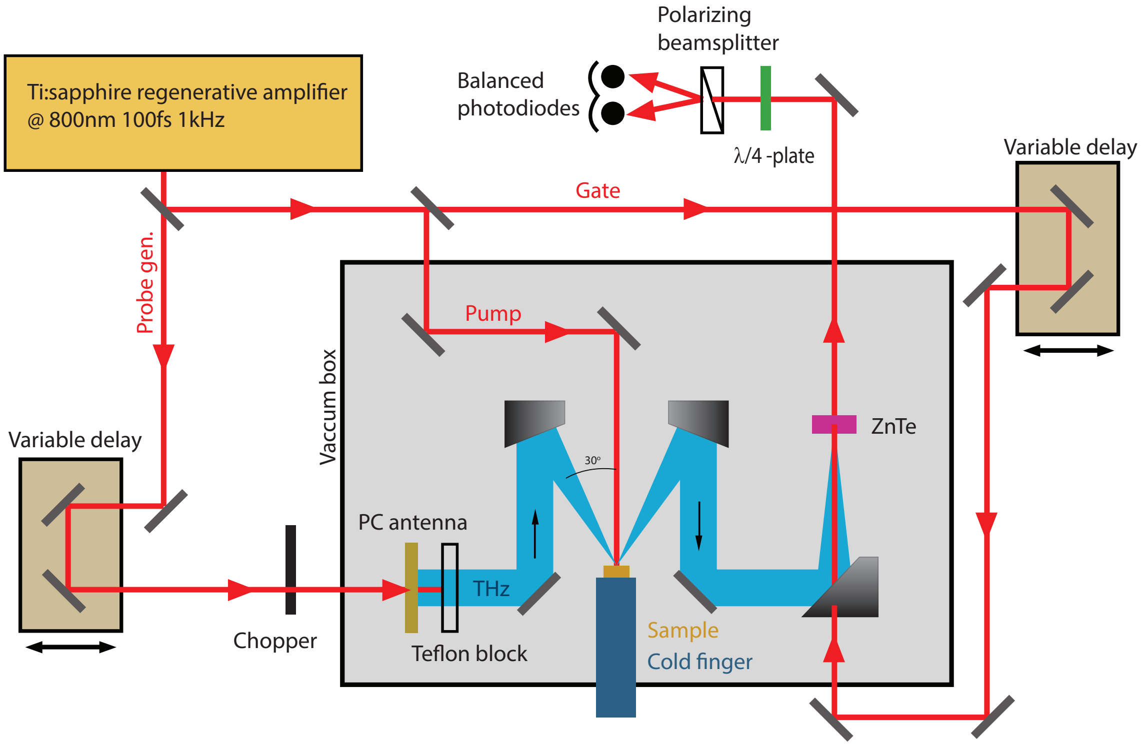

Figure 2.2: Schematic of setup for near-IR pump THz probe experiment

$$E(t) = E_0 e^{i\omega_0 t} e^{-\Gamma t^2}, \tag{2.5}$$

where ω_0 is the central frequency and the temporal $1/e^2$ width of the pulse is $\sqrt{2/\Gamma}$. The frequency profile of such pulse determined via the Fourier transform

$$E(\omega) \propto e^{-(\omega-\omega_0)^2/4\Gamma} \tag{2.6}$$

and the bandwidth of the pulse is $\Delta\omega = \sqrt{\Gamma}/2$.

2.2 High field THz generation: Tilted pulse front

After the development of the generation and detection of ultrafast THz pulses, there has been much interest and progress in being able to generate high energy single cycle THz pulses. The advent of intense THz sources has opened new chapter of THz science, allowing the exploration of non-linear phenomena in materials. The single-cycle nature of THz pulses presents unique opportunity to expose crystal structures to very large electric fields ($\sim$100 kV/cm - 1 MV/cm) without the heating affect normally caused from a dc bias and can act as an ultrafast electric- or magnetic-field switching operation over the timescale of a few hundred femptoseconds. Over the past three decades there has been significant improvement in the the generation techniques[3, 20, 27] which has largely been due to increases in generation efficiency and material choice. Two review articles by H. Hirori and K. Tanaka [31] and by H. Hafez *et. al.* [28] adequately cover the current state of intense THz generation techniques and applications.

A commonly used method for intense THz generation is through optical rectification in non-centrosymmetric media taking advantage of the second order nonlinear process described in section 2.1.2. The nonlinear material must be transparent at near-IR and THz frequencies and bear a high damage threshold in order to withstand intense generation pulses. Another important consideration is the phase matching condition in the material between the near-IR group velocity and the generated THz phase velocity. In difference frequency mixing between the two different near-IR photons, the momentum conservation equation is given by

$$\mathbf{k}(\Omega) = \mathbf{k}(\omega_1) - \mathbf{k}(\omega_2). \tag{2.7}$$

The wave vector $\mathbf{k}$ is frequency dependent upon the index of refraction within a given material. As the near-IR pulse propagates through the crystal, THz radiation is emitted at each position and depending on the phase matching condition, may be adding together coherently in phase or become out of phase over some coherence length L_c. The coherence length is define as the distance a pulse travels for the generated THz to reach a π phase change, leading to destructive interference.

In the case for ZnTe, the near-IR group velocity and THz phase velocity are equal, enabling a simple colinear experimental setup and making ZnTe a common and useful source for THz generation. Intense THz pulses up to 1.4 μJ in energy have been generated using a large aperture ZnTe crystal and very high pump enery of 48 mJ[7]. With higher pump fluences, ZnTe is prone to two photon absorption leading to free-carrier absorption of the THz pulse within the crystal, necessitating a large beam size to be below the saturation fluence. Although the THz pulse energy is quite large, it requires the use of very high powered laser systems and large diameter crystals which can be expensive and difficult to grow.

A better suited material for intense THz generation is $LiNbO_3$. The material has a much higher damage threshold and is not prone to two photon absorption, allowing higher pump fluences. However, unlike ZnTe, $LiNbO_3$ has a large mismatch between the near-IR group velocity and the THz phase velocity leading to a short coherence length and poor conversion efficiency in a colinear setup. To overcome this obstacle, a tilted pulse front technique was developed by Hebling *et al* [29], where the pump pulse continuously generates THz radiation in phase along the direction of THz output while propagating through the crystal. In order to fulfill the phase matching condition, the pump and THz pulse's propagation directions inside the crystal should make an angle $\gamma = \cos^{-1}(n^{\mathrm{gr}}_{800}/n^{\mathrm{ph}}_{\mathrm{THz}}) = 63^o$, where $n^{\mathrm{gr}_800}= 2.25$ is the group refractive index at 800 nm and $n^{\mathrm{ph}}_{\mathrm{THz}} = 4.96$ is the phase refractive index of the THz beam. A diagram of the tilted pump pulse propagating through the nonlinear crystal is shown in Fig. 2.3(a). The THz pulse front generated upon entering the $LiNbO_3$ remains in phase with the THz produced as the pump pulse travels further, thus extending the coherence length and generation efficiency. This experimental technique has been developed further over the past decade [25, 64, 30, 8] as well as the theory behind it[59].

The near-IR tilted pulse front is achieved by taking the 1st order reflection from a diffraction grating. Due to refraction of the tilt inside the crystal, the pulse front is tilted in air to an angle of $\gamma' = \tan^{-1}\left(n^{gr}_{800}\tan(\gamma)\right) = 78^o$. We used a grating with a groove density of $d = 2000$ lines/mm which had an incident and diffracted angles $\theta_i = 60^{\mathrm{o}}$ and $\theta_r = 47^{\mathrm{o}}$ determined by

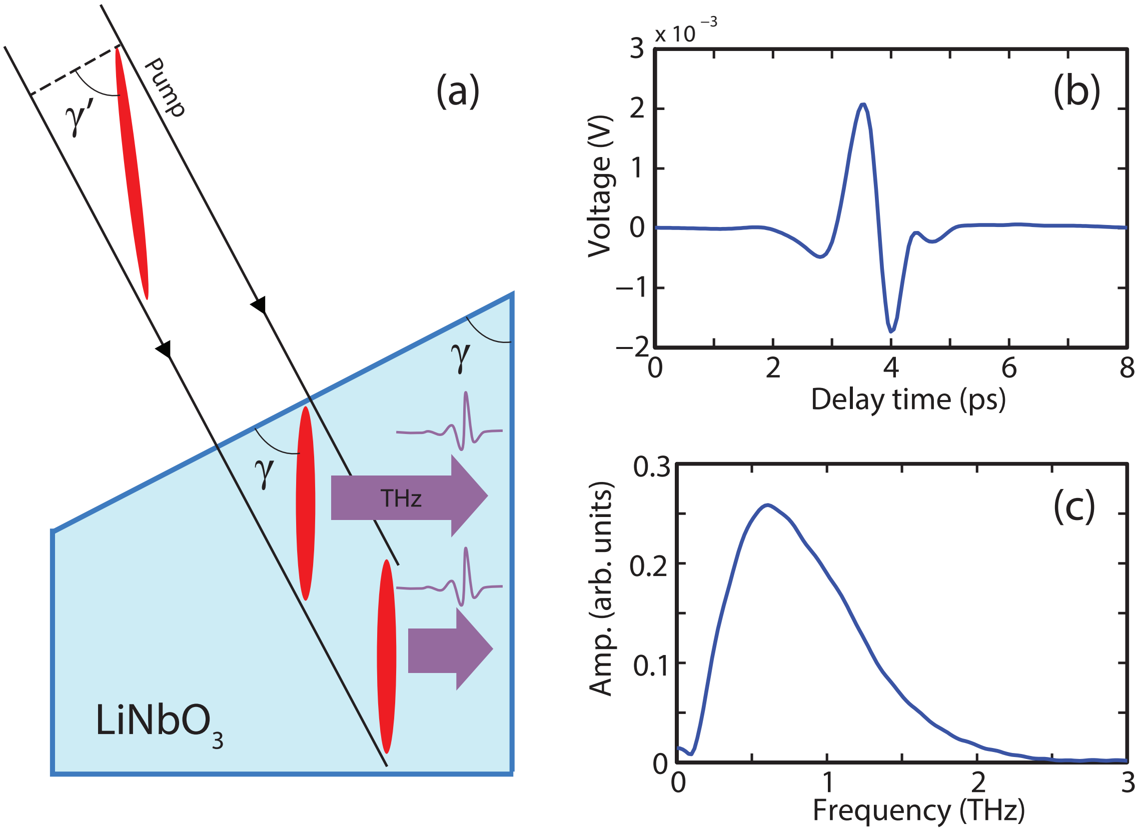

Figure 2.3: Intense THz generation using the tilted pulse front technique. Panel (a) shows the internal geometry of the pump pulse propagating through the $LiNbO_3$ crystal with a pulse front angle γ with respect to the direction of travel. The arrows show the THz generated towards the end of travel is in phase with the THz generated upon entering the crystal. Panels (b) and (c) display the time domain profile and Fourier transform of the THz pulse measured via EO sampling in a GaP crystal.

$$d\left(\sin(\theta_i) - \sin(\theta_r)\right) = m\lambda_0, \tag{2.8}$$

and the constraint of the tilt angle

$$\frac{\sin\theta_i + \sin\theta_r}{\cos\theta_r} = \tan\gamma', \tag{2.9}$$

where $\lambda_0 = 800$ nm and $m = 1$. The diffracted pulse then passes through a $\lambda/2$ waveplate for vertical polarization and is imaged onto the LiNbO$_3$ surface with a biconvex lens ($f = 80$mm). The distance from the grating to the lens and from the lens to the crystal surface is 240 mm and 120 mm respectively given a magnification of 0.5. The pulse is also shaped in advanced of the grating optic by a pair of cylindrical lens's with focal lengths $f = 100$ and -50 mm in order to compensate for horizontal broadening of the pump pulse in the crystal by a factor of $\sim 1/\cos\gamma$=2. THz radiation is emitted from the side of the crystal, 117^o from the incindent beam's direction, and reflected by a mirror and collimated using a $f = 120$ mm TPX lens. The THz pulse passes through a pair of wire grid polizers, enabling precise attenuation of the field strength, and focused onto the sample position with a $f = 101.6$ mm parabolic mirror.

2.3 Vacuum chamber construction

To study superconductors and other quantum materials requires the controlled use of cryogenic temperatures. This is usually done within a specially designed cryostat to hold the sample under vacuum and regulate the flow of liquid nitrogen and helium. Issues arise when using standard cryostats when performing optical measurements covering a broad range of wavelengths because the light must transmit through a window going from the table to the sample and back through the window to be measured. Many times we would like to be able to probe with THz light and pump with a variety of wavelengths covering THz to mid-infrared to near IR or visible.

There is simply no material for a window that does this well at all wavelengths. One way around this is to build a vacuum chamber to house the sample as well as the THz generating optics. A larger chamber will also allow the use of multiple windows for different pump and probe with materials specifically chosen to give the most transmission at that wavelength. With the THz generated and detected inside of the vacuum chamber, there is an added benefit to no loss in signal through a window or absorption from air inside the chamber.

This of course comes with added complications. With such a large volume, achieving and maintaining a suitable vacuum for cryogenic temperatures becomes problematic, especially when the chamber is filled with optics which outgas under low pressure. We decided to pursue this endeavour and design a vacuum chamber that could house all the optics for THz generation and detection as well as high field-THz generation via the tilted pulse front technique described in the previous section. We constructed a chamber 58.4 cm long by 39.4 cm wide and 22.9 cm tall which was milled out of a solid piece of aluminum (to avoid leaks through welded seems) and has an internal volume of $\sim$ 36.5 L.

Initially we had the entire chamber anodized in black to improve safety by avoiding stray beam reflections off of a smooth metallic surface. We quickly learned that anodized surfaces outgas at a much higher rate than bare aluminum since the surface is essentially porous with microscopic holes which trap oils and water moisture only to be slowly released under low pressure. After several trips back and forth to the machine to machine shop to mill off the internal anodized surface and installing a larger turbo pump, we were finally able to reach low enough pressures for experiments . We use a 300 l/s turbo pump which is attached directly to the side wall of the vacuum chamber and are able to achieve pressures $\sim$ 2x10^{-6} mbar after pumping on the pumping on the system overnight. The cryostat used is a modified LT3 model from Advanced Research Systems mounted on a x-y-z stage and is secured to the chamber via a metallic bellow which allows precise movement of the sample position. Figure 2.4 shows the internal optics within the vacuum chamber and external mounting system of the cryostat and turbo pump. We have found that the vibration from the pump has a negligible effect on the sample position and noise of the measurement.

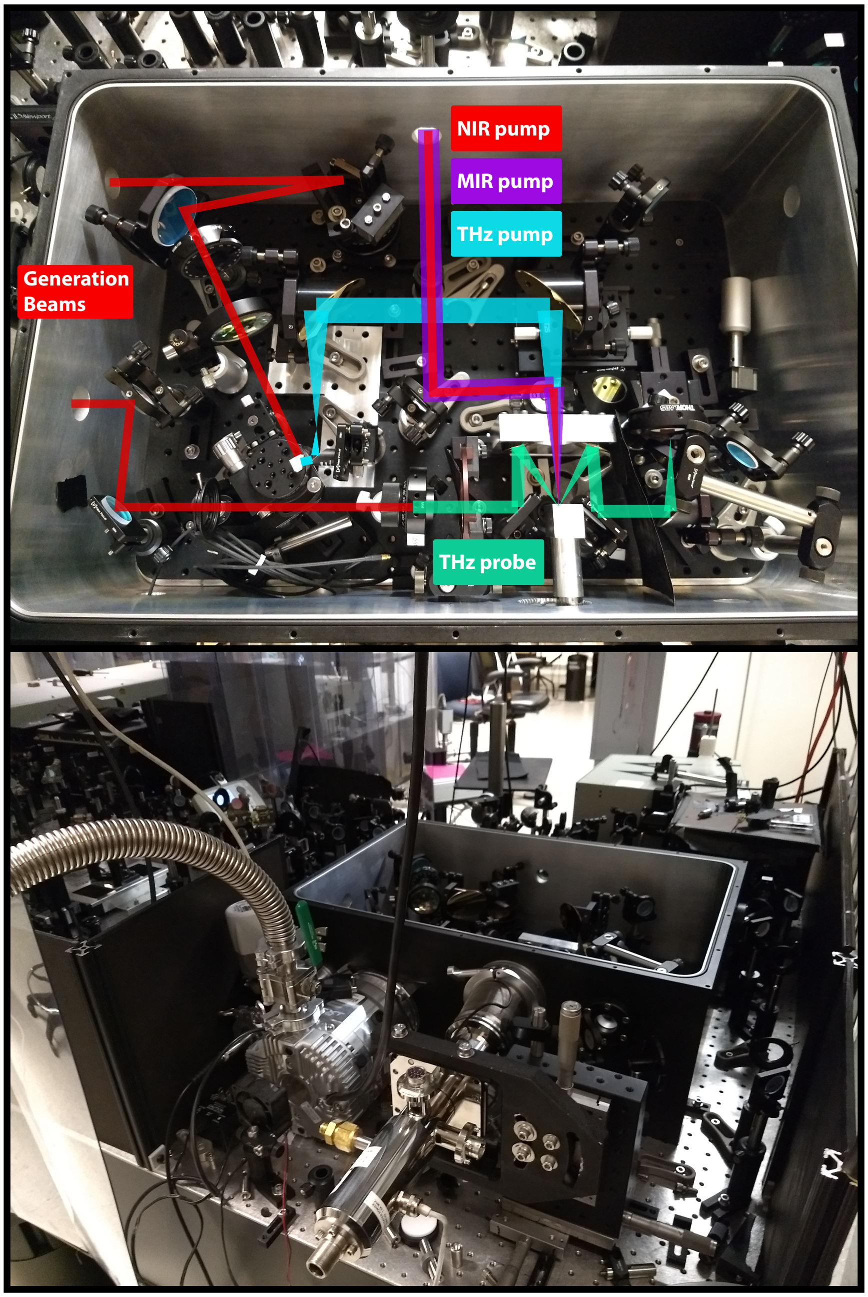

Figure 2.4: Vacuum chamber housing the THz spectroscopy experiment. (Top) Internal optics used for generating and detecting THz pulses as well as multiple beam paths setups for different pump configurations. (bottom) Vacuum chamber sitting on optical table with turbo pump and cryostat attached.

Chapter 3

Time domain THz spectroscopy analysis

3.1 Layered Model

The photo-induced change $\Delta E_s(t,\tau)$ in the reflected electric field was measured at various pump probe time delays τ, over the temporal window t of the THz pulse. The quantity $\Delta E_s(t,\tau) = E_{s,\text{pumped}}(t,\tau)E_{s,\text{unpumed}}(t,\tau)$ was acquired at each delay time τ by using a lock-in triggered by the modulation of the pump pulse with a mechanical chopper. The unpumped electric field was measured 40 ps before the arrival of the pump pulse.

The raw photo-induced changes ΔE measured in the reflected field require further processing to extract the complex optical properties of the excited region. The penetration depth mismatch between 800 nm pump ($\sim$400 nm) and THz probe ($\sim$100-300 μm) results in a relatively small change in ΔE ($\sim$1-3 %) after photo-excitation and is considered when modeling the THz response. We model the photo-excited region as a thin layer with a thickness of d = 400 nm on top of an unperturbed bulk containing the material properties of the sample in equilibrium before the arrival of the pump pulse. The total complex reflection coefficient $\tilde{r}_{\text{tot}}(\omega)$ from the layered system is the summation of all internal reflections displayed in Fig. 3.1 and can be expressed in closed form as: [18]

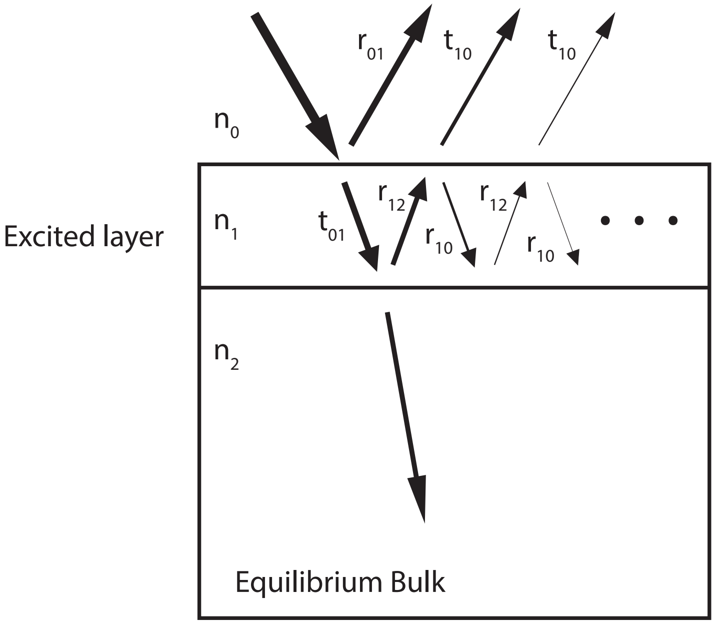

Figure 3.1: Schematic drawing of thin layer model. In this model the thin excited layer sits on top of the bulk crystal containing the equilibrium optical properties.

$$\tilde{r}_{\text{tot}}(\omega) = \frac{r_{01} + r_{12}e^{i2\delta}}{1 + r_{01}r_{21}e^{i2\delta}} \tag{3.1}$$

$$\delta = \frac{2\pi d}{\lambda}\sqrt{n_1^2 - \sin\theta_1} \tag{3.2}$$

where $\tilde{r}_{01}$ and $\tilde{r}_{12}$ are the reflection coefficients from the front and backside of the excited layer, respectively, and λ is the THz wavelength. The phase accumulation as the THz pulse travels through the excited layer is given by δ. The complex reflection coefficient $\tilde{r}_{tot}(\omega,\tau)$ was determined from the experimentally measured quantities $\Delta\tilde{E}_s(\omega,\tau)$ and $\tilde{E}_s(\omega)$ using the relation

$$\tilde{r}_{\text{tot}} = \tilde{r}_{\text{eq}}(\omega)\left[\frac{\Delta\tilde{E}_s}{\tilde{E}_s} + 1\right] \tag{3.3}$$

were $\tilde{r}(\omega)$ is the equilibrium reflection coefficient. A numerical solution to the above Fresnel equation was found, returning a value for the complex index of refraction $\tilde{n}_1(\omega,\tau)$ of the excited layer. We calculate the complex conductivity of the photo-excited layer

$$\tilde{\sigma}(\omega,\tau)=\frac{\omega}{4\pi i}\left[\tilde{n}_1(\omega,\tau)^2-\varepsilon_\infty\right] \tag{3.4}$$

using $\varepsilon_\infty = 4.5$ as a standard value for the cuprates.

Chapter 4

Photo-enhanced metastable c-axis electrodynamics in stripe-ordered cuprate $La_{1.885}Ba_{0.115}CuO_4$

4.1 Introduction

High-temperature superconductivity in the cuprates can coexist or compete with a multitude of other phenomena, including charge and spin order, pair density waves, and the pseudogap[73, 47, 12, 15] all of which have observable signatures in the linear or transient electrodynamic response[5]. A key question for the cuprates is the extent to which the underlying interactions can be manipulated to alter the macroscopic properties. Ultrafast pump probe spectroscopy provides a unique means to initiate and interrogate non-equilibrium dynamics and property control in superconductors[26, 49].

Evidence of transiently enhanced interlayer tunneling has been reported in several cuprates following selective phonon pumping[21, 34, 54] or intense near infrared excitation[52]. In these experiments, the c-axis Josephson plasma resonance (JPR) serves as a reporter of the interlayer tunneling which, in general, scales with the superfluid spectral weight[67]. Upon applying intense near infrared pump excitation starting above the transition temperature T_c, Nicoletti et. al. observed a blueshift of the plasma resonance relative to the below T_c equilibrium response. The plasma resonance decayed after several picoseconds and was interpreted in terms of transient superconductivity[52]. Similar dynamics were subsequently observed in both $La_{2-x}Ba_xCuO_4$ and $YBa_2Cu_3O_{6+x}$ over a range of doping levels and excitation conditions. More recently, in $La_{2-x}Ba_xCuO_4$ ($x = 0.095$), a longer lived (> 50 ps) collective response was observed subsequent to photoexcitation at $T < T_c$ in which the JPR appeared to split into two distinct longitudinal modes[80], reminiscent of the static electrodynamic response in bilayer cuprates[74, 63, 39]. Further no pump-induced effect was observed above T_c. Notably, the $x = 0.095$ material does not exhibit robust charge or stripe order[35].

4.2 Methods

In this report, we clarify the details of the photoinduced order parameter control in the cuprates, by performing temperature and fluence dependent c-axis measurements on materials with equilibrium signatures of phase competition. We present near-infrared pump, THz probe experiments of $La_{2-x}Ba_xCuO_4$ ($x = 0.115$), for which we observe distinct dynamics above and below T_c. The doping $x = 0.115$ is close to the anomalous $x = 1/8$ composition where 3D superconductivity is maximally suppressed by robust charge and stripe order[47],[42, 24, 72]. At $x = 0.115$, charge order, spin order and 3D superconductivity onset at $T_{co} = 53$ K, $T_{so} = 40$ K, and $T_c = 13$ K, respectively[35]. In this compound T_c is high enough to enable initiating dynamics from within the superconducting state. The $La_{1.885}Ba_{0.115}CuO_4$ crystal was cut and polished to expose the a-c plane with a large area of 5 mm x 5 mm. Temperature dependent FTIR measurements were carefully performed to provide a baseline static characterization of the electrodynamic response.

The c-axis properties were probed with broadband THz pulses generated from a commercial GaAs based photo-conductive antenna using incident light from a 1 kHz Ti:Sapphire regenerative amplifier. The THz pulses produced have a usable bandwidth from 0.15-2 THz which allowed a measurement of the equilibrium Josephson plasma resonance (JPR) near 0.2 THz for x = 0.115 doping. A schematic of the optical pump-THz probe measurement in reflection is shown in Fig. 2.2 in chapter 2.

The probe pulses were focused onto the sample at an incident angle of 30 degrees with the electric field polarized along the c-axis. The THz pulses were collected after the sample and measured via electro-optic sampling with an 800 nm gate pulse in a 2mm thick ZnTe crystal. The LBCO crystal was photoexcited with 100 fs, 800 nm wavelength pulses, polarized along the c-axis with a beam diameter of 6 mm FWHM to ensure a uniform excitation across the sampled region.

The equilibrium c-axis reflectivity above T_c was characterized with broadband FTIR measurements at 30 K which is displayed in Fig. 4.1. The equilibrium complex index of refraction $\tilde{n}(\omega)$ was determined by fitting the reflectivity curve with Drude-Lorentz oscillators placed at known IR phonon frequencies[33]. The fit was accomplished using the software package RefFIt$^{\text{TM}}$ and is shown in Fig. 4.1. A small Drude component was added to give a dc conductivity $\sigma_1(\omega = 0) \sim 3\ \Omega^{-1}\text{cm}^{-1}$ at 30 K to match previous transport measurements[33, 37].

The reflection coefficient of a material is given by $\tilde{r}(\omega) = \tilde{E}_s(\omega)/E_i(\omega)$ where $\tilde{E}_s(\omega)$ is the electric field reflected off the sample and $\tilde{E}_i(\omega)$ is the incident field. By measuring the THz waveform $E_s(t)$ via electro-optic sampling, we take the Fourier transform to obtain $\tilde{E}_s(\omega)$. The reflection coefficient was then determined at 7 K by measuring $\tilde{E}_{s,7\text{K}}(\omega)$ and using the relation

$$\tilde{r}_{7\text{K}} = \frac{\tilde{E}_{s,7\text{K}}(\omega)}{\tilde{E}_{s,30\text{K}}(\omega)} \tilde{r}_{30\text{K}} \tag{4.1}$$

The static and dynamic reflectivity of LBCO were measured as a function of temperature and fluence using terahertz time-domain spectroscopy (0.15-2 THz). As shown in Fig. 4.2(a),

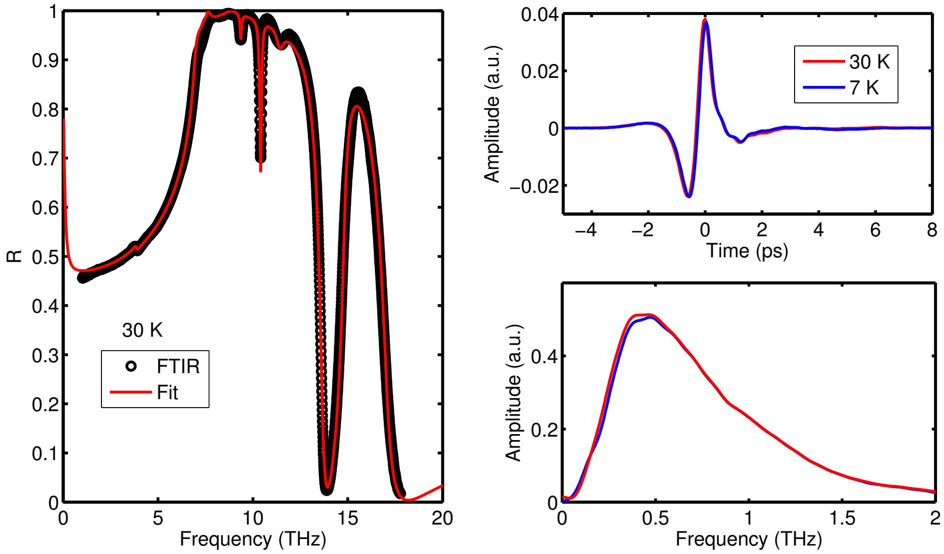

Figure 4.1: (a) c-axis reflectivity FTIR data taken at 30K with fit plotted as the red curve. (b) Time domain profile of THz pulse reflected from the sample at 30K and 7K. (c) Fourier transform of the time domain pulses in panel (b).

both the near-infrared pump (1.55 eV) and the THz probe pulses are polarized along the c-axis. The static THz reflectivity is plotted in Fig. 4.2(b), showing a flat response at 30 K (grey line, with a slight upturn below 0.5 THz). In the superconducting state (7K, blue curve) a sharp reflectivity edge emerges around 200 GHz, a hallmark of the inter-layer JPR effect in agreement with previous studies for this doping[52].

4.3 Results

For the dynamics measurements, we first performed one-dimensional scans, where the photoinduced change in the peak electric field of the single-cycle THz pulse ($\Delta E/E$) is measured as a function of pump-probe delay. This raw unprocessed data unambiguously highlights important features of the electrodynamic response. Figure 4.2(c) plots one-dimensional scans ($\Delta E/E$ peak scans) for various fluences, starting from an initial temperature of 7K, well into the superconducting state. The dynamics exhibit a long-lived response with an initial risetime of

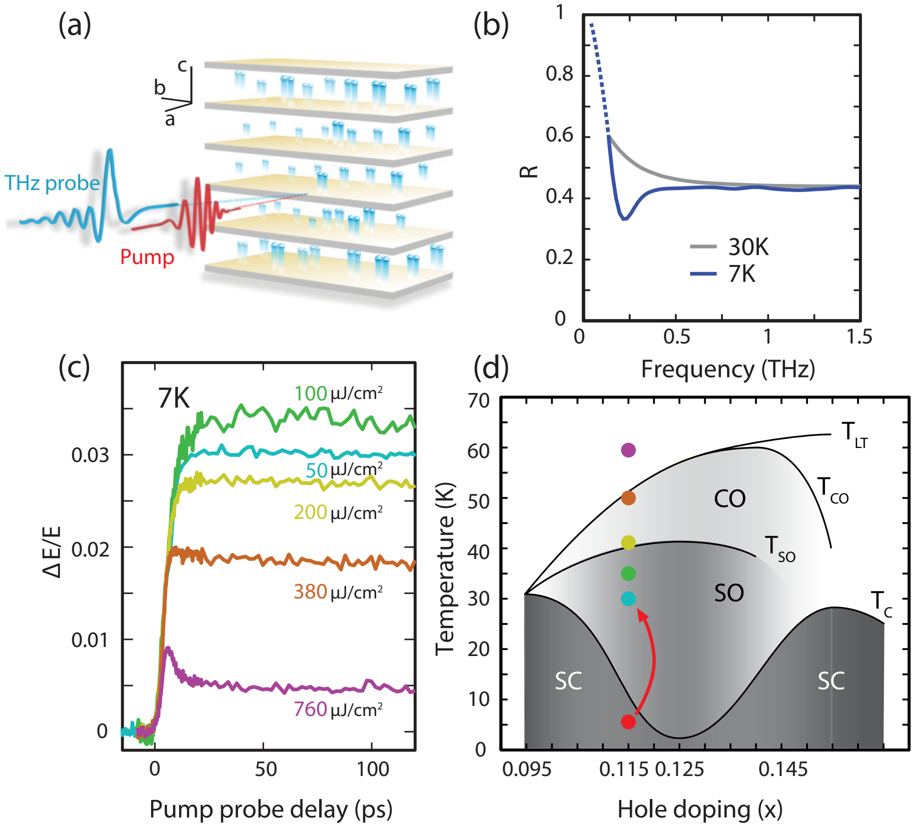

Figure 4.2: (a) Schematic of the 1.55 eV pump THz probe experiment on LBCO crystal with pump and probe polarization along c-axis. The illustration depicts the superconducting state with cooper pairs tunneling along the c-axis. (b) Equilibrium THz reflectivity above and below TC at 30 K and 7 K, respectively. The dotted line is beyond our experimentally accessible spectral range and is a guide to the eye. (c) Time dependent relative change in the THz electric field amplitude after excitation at various pump fluences (at 7 K). (d) Temperature versus hole doping phase diagram of $La_{2-x}Ba_xCuO_4$ (reproduced from Ref. [35]). Regions of the phase diagram include bulk superconductivity (SC) at onset temperature Tc, spin ordering (SO) at temperatureT_{so}, charge ordering at T_{co}, and low-temperature structural transition TLT. The initial temperature at 7 K for x = 0.115 is plotted in red, and the color dots mark the estimated lattice temperature after pump excitation and e-ph thermalization has occurred (colors corresponding to pump fluences shown in panel (c)).

several picoseconds. The magnitude of the $\Delta E/E$ signal slightly increases from 50 to 100 μJ/cm^2, followed by a strong decrease in amplitude at higher fluences up to 760 μ/cm^2. The observed fluence dependence indicates dynamics that are distinct from a photoinduced decrease in the condensate density with a commensurate increase in the quasiparticle density. In that scenario, $\Delta E/E$ would increase in magnitude with increasing fluence.

Calculations using the two-temperature model of the initial electron-phonon (e-ph) thermalization (see SI Appendix, section S3 for details) indicate a rise in the final temperature that increases with fluence (after several picoseconds when the plateau in the data in Fig. 4.2(c) is reached). Figure 4.2(d) displays the phase diagram of LBCO (reproduced from Ref. [35]) with color coded dots (corresponding to the fluences used in Fig. 4.2(c)) indicating the final temperature after thermalization. Clearly, the amplitude of $\Delta E/E$ decreases with increasing fluence as $T_{\rm co}$ is approached after the initial e-ph thermalization. This indicates that the strongest photo-induced response occurs for fluences that do not heat the sample above $T_{\rm co}$. We refer to 50 380 μJ/cm^2 as the low fluence regime where the quasi-equilibrium temperature stays below $T_{\rm co}$. The data in Figs. 4.3 and 4.4 reveal that the dynamics are dramatically different for low- and high-fluence (>380 μJ/cm^2) regimes spanning $T_{\rm co}$. The difference in dynamics is evident in Fig. 4.21(c), where the 760 μJ/cm^2 data exhibits an exponential decay in contrast to the plateau apparent in the low fluence data.

We now discuss the full spectroscopic response of the dynamics, considering first low fluence optical excitation of LBCO (100 μJ/cm^2) obtained starting from an initial temperature of 7 K. The optical properties of the photo-excited region were extracted using a layered model to account for the penetration depth mismatch between the pump and probe beams (see SI Appendix, section S2). Figure 4.3(a) shows the photoinduced reflectivity (blue curve at 10 ps, red curve at 300 ps), revealing a large reflectivity increase extending out to 1 THz, corresponding to an increase in the plasma frequency from 0.2 to 0.9 THz. This is more clearly revealed in Figs. 4.3(b) and (c) showing the loss function -Im(1/ε) (where $\varepsilon = \varepsilon_1 + i\varepsilon_2$ is the c-axis dielectric response)

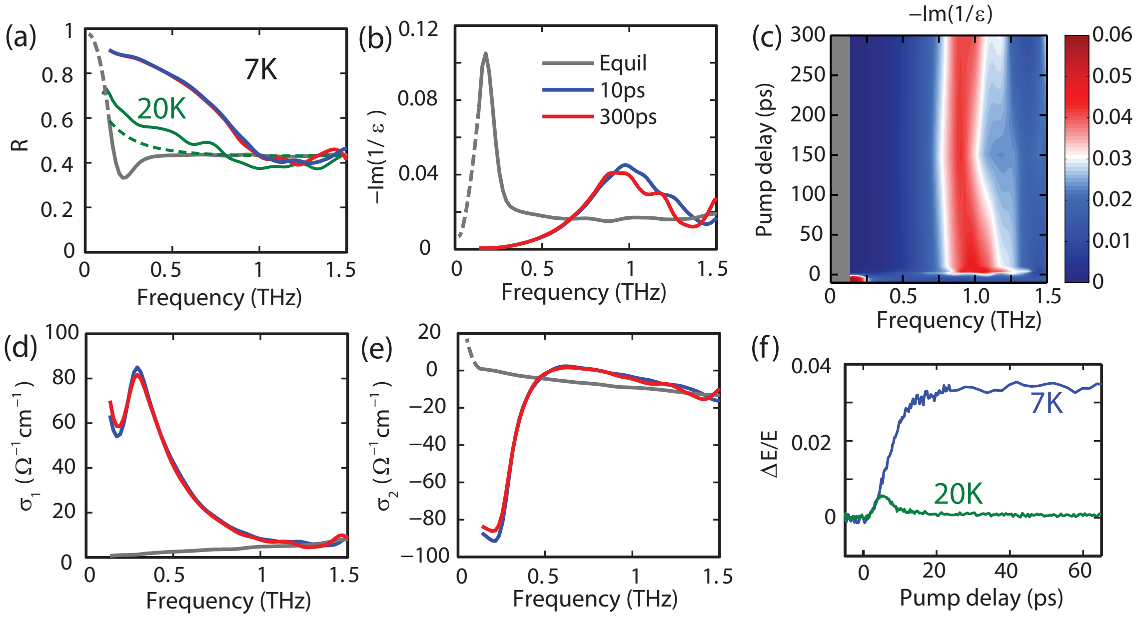

Figure 4.3: Extracted c-axis THz optical properties of LBCO at different pump-probe delays after photo-excitation (colored) with 100 μJ/cm^2 and at equilibrium (grey). All data has been taken at 7 K below T_c except for the green curves in panels (a) and (f) which were taken at 20 K. (a) Reflectivity at 7 K before (grey) and after photo-excitation (colored) at different pump-probe delays. Plotted in green is the equilibrium (dotted) reflectivity and largest photo-induced change (solid) in reflectivity at 20 K. (b) Loss function -Im(1/ε). Dashed grey line is beyond our spectral resolution and is a guide to the eye. (c) Spectral evolution of the loss function after photo-excitation. (d)-(e) Real and imaginary parts of the THz conductivity. (f) Peak of $\Delta E/E$ THz transient after photo-excitation at 7 K and 20 K.

which peaks at the plasma frequency. Importantly, there is no sign of decay of the photo-induced state over the measured temporal window, indicating a metastable state that persists beyond 300 ps. Figure 4.3(d) and (e) show the associated c-axis optical conductivity ($\sigma = \sigma_1 + i\sigma_2$) highlighting an important observation. Namely, there is a peak in σ_1 at 0.3 THz signifying dissipation in the c-axis THz transport. In contrast, in equilibrium for a superconductor, σ_1 at frequencies greater than zero but less than twice the superconducting gap approaches zero (solid grey line in Fig. 4.3(d)). This origin of the peak in σ_1 arising after photoexcitation will be discussed below. Finally, the solid green line in Fig. 4.3(a) shows the spectral response at 10 ps delay for a fluence of 100 μJ/cm^2 taken at an initial temperature of 20K that is, above T_c. There is an increase in the reflectivity, arguably with the development of a weak plasma edge. However, as shown in Fig. 4.3(f), the response is much smaller and shorter lived in comparison to dynamics initiated from within the superconducting state. In short, the emergence of a robust metastable state upon low fluence photo-excitation requires starting from the superconducting state while remaining below T_{co} after e-ph thermalization.

To complete the data discussion, we now consider the high fluence dynamics. Figure 4.4 shows the spectroscopic results for high fluence excitation at 9 mJ/cm^2 which leads to a final temperature greater than T_{co}. Fig. 4.4(a) reveals an increased reflectivity starting from an initial temperature of 30 K. At early times a broad peak emerges in the loss function (shown in Fig. 4.4(b) and (c)) that rapidly broadens and decays on a 10 ps timescale. There is a corresponding increase in σ_1 and σ_2 (Fig. 4.4(d) and (e)), though there are no well-defined peaks as for the low fluence results. Fig. 4.4(f) reveals the rapid decay in the transient $\Delta E/E$ with 9 mJ/cm^2 excitation, with the inset showing a saturation of the dynamics with increasing fluence. The plateau in the $\Delta E/E$ scans following the initial exponential decay is presumably associated with heating, leading to a broad and featureless optical conductivity from 0.1 1.5 THz. The broadened plasma edge that appears after the arrival of the pump pulse is qualitatively in agreement with the previous study by Nicoletti et. al.[52]. Given the relatively small value of σ_1, this could

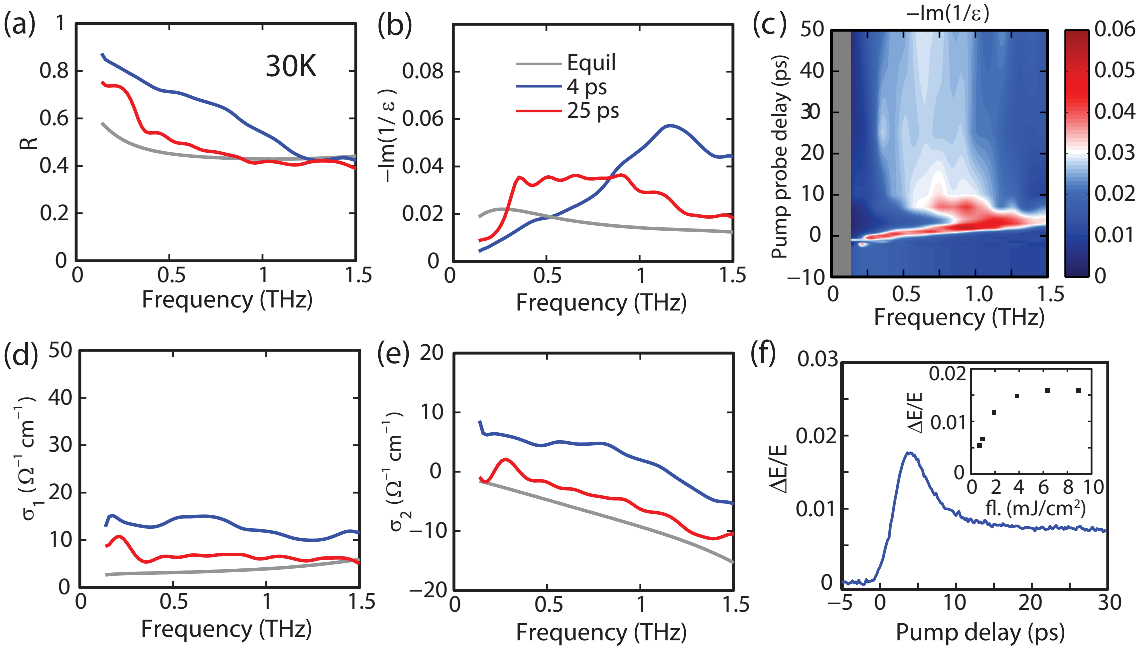

Figure 4.4: Extracted c-axis THz optical properties of LBCO at different pump-probe delays after photo-excitation (colored) with 9 mJ/cm^2 and at equilibrium (grey). All data taken at 30 K above T_c and below T_{co}. (a) Reflectivity and (b) loss function, -Im(1/ε) at different pump probe delays. (c) Spectral evolution of the loss function after photo-excitation. (d)-(e) Real and imaginary parts of the THz conductivity at different pump probe delays. (f) Time dependent relative changes in THz electric field after photo-excitation. The inset displays the maximum $\Delta E/E$ value at 30 K as a function of pump fluence.

indicate the presence of enhanced superconducting correlations associated with the unambiguous transient blueshift of the plasma frequency. Summarizing, the high fluence transient response evolves at temperatures above T_{co} and is short lived, in contrast to the low fluence metastable results presented in Fig. 4.3, implying that the two features correspond to distinct states.

4.4 Discussion

We now discuss the origin and nature of the low fluence photoinduced metastable electrodynamic response (Figure 4.3). For 100 μJ/cm^2, the temperature following e-ph thermalization is 35 K. In equilibrium, 35 K is within the charge ordered, non-superconducting region that is spectrally featureless at THz frequencies. In contrast, the low fluence metastable state produced by c-axis excitation exhibits unique spectroscopic features in the loss function -Im(1/ε) (Fig. 4.3(b) and (c)) and conductivity (Fig. 4.3(d) and (e)) that are indicative of a non-equilibrium metastable state. Importantly, the plasma frequency (ω_p) is blueshifted by a factor of 4.5 upon photoexcitation (from 0.2 to 0.9 THz) corresponding to an increase of the low energy spectral weight (Σ) by a factor of 20 (i.e., $\Sigma \propto \omega_p^2$). This is a robust observation, independent of the microscopic origin of the electrodynamic response. Additionally, the spectral weight must originate from energies beyond the 1.5 THz regime probed here because the equilibrium condensate spectral weight (Fig. 4.5(a)) is far too small to account for the factor of 20 increase. A change in the c-axis response may also arise from structural distortions affecting interlayer coupling independent of a change in the in-plane superfluid density[66]. Although our measurements are not directly sensitive to structural distortions, we estimate the metastable phase to be at 35 K which is still below the low temperature orthorhombic to tetragonal transition occurring at 53 K[33]. As such, this is not likely to be the cause of the increase in Σ. We next show that a more likely scenario for the increase in Σ is photoinduced collapse of charge/stripe order whereby spectral weight originally at energies above the CDW gap scale is made available for enhanced c-axis transport.

A well-known approximate scaling relationship (valid for both c-axis and ab-plane) for the cuprates is $\rho_0 = 120\sigma_{dc}T_c$, where ρ_0 is the superfluid density ($\propto \omega_p^2$) and σ_{dc} is the zero frequency conductivity measured just above T_c[32]. Figure 4.5(a) shows the product $\sigma_{dc}T_c$ versus ρ_0 for x = 0.115 doping measured in this study, and for x = 0.95 and x = 0.145 taken from Ref. [33]. For x = 0.115 at 7 K, the JPR appears near the renormalized superconducting plasma frequency ω'_p = 6.7 cm^{-1} (200 GHz). The unscreened plasma frequency is given by $\omega_p = \omega'_p\sqrt{\varepsilon_\infty}$ ($\varepsilon_\infty \sim 30$) giving a superfluid density $\rho_0 \equiv \omega_p^2 = 1.3\text{x}10^3$ cm^{-2} (This is taken to be very near the superfluid density at T = 0 K). The conductivity just above T_c = 13 K is taken as $\sigma_{dc} \sim 0.8\ \Omega^{-1}\text{cm}^{-1}$, estimated from transport measurements on a similar doping of x = 0.1124. As seen in Fig. 4.5(a), the x = 0.115 doping is consistent with $\rho_0 = 120\sigma_{dc}T_c$ plotted as a dashed line. We now extend this

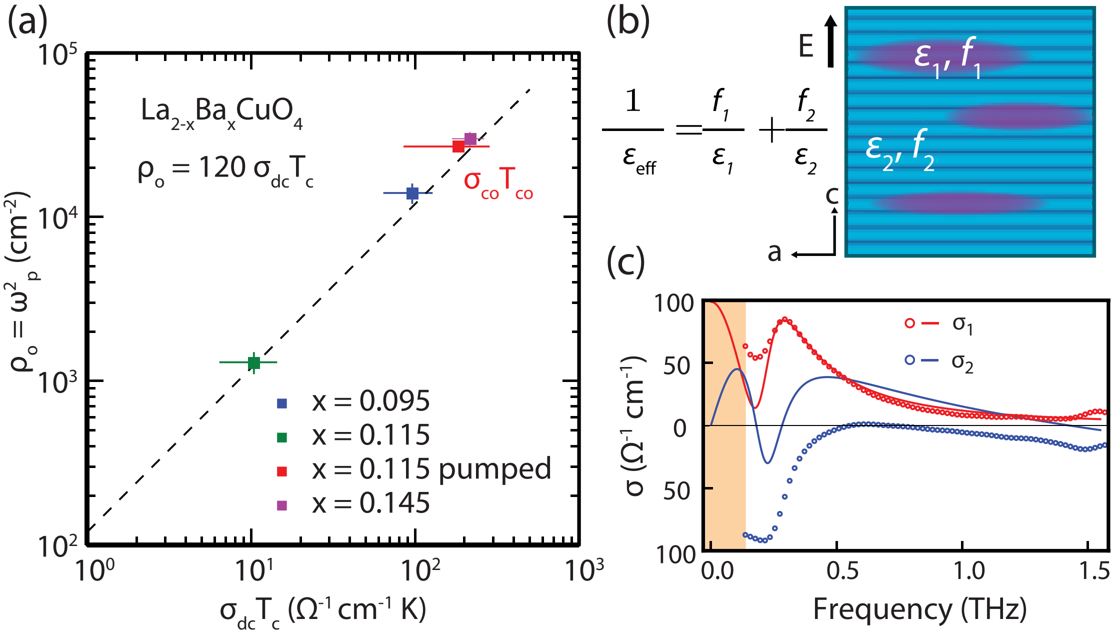

Figure 4.5: (a) Plot of the superfluild density s versus the product of the zero frequency conductivity (σ_{dc}) and the superconducting transition temperature T_c for several dopings of LBCO (dc is the conductivity measured just above the superconducting transition). The values for $x = 0.95$ and $x = 0.145$ were taken from Ref. [33]. The dashed line is the universal scaling relation for cuprates $\rho_s = 120\sigma_{dc}T_c$ found by Homes et. al. [32] (b) Schematic of anisotropic effective medium theory along the c-axis with regions of different dielectric constants ε_1 and ε_2 and filling fractions f_1 and f_2 respectively. The superconducting volume is depicted with dark ellipses and the transformed region is in blue. (c) Real (red) and imaginary (blue) parts of the THz conductivity after photo-excitation with 100 μJ/cm^2 at 7 K. Experimental data is plotted with dots and the effective medium model with solid lines.

concept to the photoinduced metastable state which, as described above, exhibits a large increase in spectral weight.

From the photoinduced blueshift of the plasma edge ($\omega_e' \sim 0.9$ THz or 30 cm^{-1}) it is possible to determine the photoinduced density ρ_e. This estimate from experimental data gives $\rho_e = 2.7\text{x}10^4$ cm^{-2}, yielding $\rho_e/\rho_0 \sim 20$ as mentioned above. We now assume the validity of the scaling relation $\rho_e = 120\sigma_{co}T_{co}$ where $\sigma_{co} \sim 3\ \Omega^{-1}\text{cm}^{-1}$ is the conductivity just above the charge ordering temperature ($T_{co} = 53$ K). From this we obtain $\rho_e/\rho_0 \sim (\sigma_{co}T_{co})/(\sigma_{dc}T_c) \sim 15$, in reasonable agreement with experiment. The product $\sigma_{co}T_{co}$ is plotted in Fig. 4.5(a) as a red data point and lies on the dashed line given by $\rho_s = 120\sigma_{dc}T_c$. This suggests that c-axis spectral weight initially tied up in charge order is released upon photoexcitation leading to the blueshift of the plasma edge. We note that the precise microscopic reason for the photoinduced collapse of charge order upon c-axis interband excitation is not understood and is a topic for future investigation, beyond the scope of the present study.

The peak in the loss function cannot be simply described as an enhanced plasma edge with increased interlayer tunneling arising from the collapse of the charge order. This is because we have a peak in σ_1 at a non-zero frequency (Fig. 4.3(d)). In principle, two inequivalent junctions (with different inter-layer spacing) do yield two distinct longitudinal JPRs at different frequencies. For example, Sm doped $La_{2-x}Sr_xCuO_4$ (LSCO), is composed of a stack of inequivalent Josephson junctions. Out of phase oscillations of the two longitudinal modes result in a transverse mode with a resonance frequency intermediate to the two JPRs with a corresponding peak in σ_1[39, 75]. In such a case, the spectral weight would be associated with a pure superfluid response, which is certainly intriguing since our LBCO sample is (as discussed above) at 35 K following e-ph equilibration (i.e. $\sim 2.7T_c$). It is, however, not clear how photoexcitation could lead to uniform creation of a well-defined microscopic bi-layer structure, though spectroscopic aspects of this are present in the non-charge ordered LBCO ($x = 0.095$)[80]. However, for $x = 0.115$, charge order collapse plays a dominant role as described above. As such, we consider an alternative scenario based on photoinduced mesoscopic inhomogeneity.

The simplest effective medium theory for an anisotropic layered crystal (appropriate to c-axis cuprates) is schematically depicted in Fig. 4.5(b) where regions are transformed into a metastable state (blue) while others remain untransformed (dark ellipses). The domain boundaries of the two different phases are along the a-b plane giving rise to regions with differing c-axis coupling strengths. The dark horizontal stripes represent the insulating barriers between CuO_2 planes which give rise to the Josephson effect along the c-axis. The effective dielectric response eff is given as $1/\varepsilon_{eff} = f_1/\varepsilon_1 + f_2/\varepsilon_2$ where f_1 and f_2 are the volume fractions corresponding to regions with complex dielectric function ε_1 and ε_2, respectively[50]. Taking f_1 as the superconducting volume fraction (having the 7K equilibrium response), and f_2 as a Drude response (with a finite scattering rate of 0.36 THz) yields the fit to the experimental data shown in Fig. 4.5(c). For additional details regarding the model and fit we refer the reader to SI Appendix, section S4. Notably, the peak in σ_1 corresponding to a photoinduced transverse mode is accurately reproduced with this model taking $f_1 = 0.02 \pm 0.01$ and $f_2 = 0.98 \pm 0.01$. While the general features of σ_2 are reproduced by the effective medium model, an exact fit was not possible. We note that errors in extracting σ_2 from experiment are generally more difficult in comparison to σ_1 as this depends sensitively on changes in phase of the terahertz pulse.

Taking the fits as representative of the photoinduced state leads to some interesting conclusions. First, the preponderant component consisting of a Drude response is consistent with the picture presented above that the pump destroys the charge/spin order. Second, a small but non-negligible superconducting volume fraction ($\sim$2%) is required to obtain the spectral response in Fig. 4.5(c). This indicates that even though the temperature is more than two times greater than the equilibrium T_c, regions of superconductivity persist. Furthermore, the Drude response (associated with f_2) is anomalous as it exhibits a small scattering rate of 0.36 THz. This is surprising for a non-superconducting c-axis response and has not been observed in the equilibrium c-axis response for any cuprate material. We suggest that the origin of this enhanced response arises from incipient superconducting correlations that enhance the c-axis conductivity as has been theoretically discussed[2, 60]. This is consistent with the experimental observation that the observed metastability requires starting from an initial superconducting state and that a non-zero superconducting volume fraction persists after photoexcitation. Previous pump probe studies on the cuprates have also observed long-lived dynamics after photo-excitation of the superconducting state, although the fluence dependence differs from what we have observed[78, 43, 44]. In these studies the slow relaxation rate of the quasiparticles is described by a persistent phase separation along the CuO_2 planes which may be a general feature in the cuprates and responsible for the long-lived state we observe. It will be important to pursue comparative experimental studies as a function of doping and excitation fluence gain additional insight into the nature of the metastability we have observed in LBCO. Such studies will also benefit from theoretical investigations of the origin of metastability in materials with competing order32.

4.5 Conclusion

In summary, low fluence photo-excitation favors the establishment of a novel long lived state with superconductivity playing an important role. Additional experiments are required to fully characterize the observed metastable response and the effective medium description of mesoscale inhomogeneity that includes a superfluid response. Our results raise crucial theoretical questions including the origin of the superconductivity and the physics and surprisingly long lifetime of the metallic state. The observed long lifetime bodes well for performing additional experiments, including time-resolved nanoscopy to spatially resolve the photoinduced state.

4.6 Effective medium model

We model the photo-excited layer in LBCO as inhomogeneous where regions are transformed into a metastable state while the remaining stays untransformed. The most simplified model is depicted in figure 4(b) of the main text where domain boundaries of the two phases are along the a-b plane. If the typical length scale of the inhomogeneity is much smaller than the thickness d of the photo-excited layer, one could treat the latter as a 3D uniform medium whose dielectric function along the c-axis is described by the effective medium formula[50]

$$\frac{1}{\varepsilon_{\mathrm{eff}}} = \frac{f_1}{\varepsilon_1} + \frac{f_2}{\varepsilon_2}, \tag{4.2}$$

where ε_{eff} is the effective dielectric function and

$$\varepsilon_1 = \varepsilon_\infty \left(1 - \frac{\omega_{j1}^2}{\omega^2}\right) + \frac{4\pi i}{\omega}\sigma_t, \tag{4.3}$$

$$\varepsilon_2 = \varepsilon_\infty \left(1 - \frac{\omega_{j2}^2}{\omega(\omega + i\gamma_2)}\right) \tag{4.4}$$

are the dielectric functions of the original and transformed regions with corresponding volume fractions f_1 and f_2 respectively. Equation 4.3 describes the optical conductivity of a Josephson array embedded in a dielectric environment ε_∞ with ω_{j1} being the strength of the equilibrium JPR and σ_t the dissipative interlayer tunneling conductivity. The transformed region is described by a Drude type response in Eq. 4.4 with plasma strength ω_{j2} and scattering rate γ_2.

The experimental data (red and blue dots) and effective medium model (solid curves) are plotted in Fig. 4.6 in terms of the optical conductivity. The values of the parameters used in the model are: $\omega_{j1} = 1.8$ THz, $\sigma_t = 0.38\ \Omega^{-1}\text{cm}^{-1}$, $f_1 = 0.22$, $\omega_{j2} = 1.45$ THz, $\gamma_2 = 0.26$ THz, $f_2 = 0.978$ and $\varepsilon_\infty = 30$. The difference in filling fractions suggests that most of the excited layer is transformed but a small remaining superconducting fraction is necessary to match the experimental results. The dashed lines in Fig. 4.6 are the model plotted with a $\pm 1\%$ difference in filling fractions which is taken to be the error on f_1 and f_2.

4.7 Acknowledgements

The work in this chapter has been published in *Proceedings of the National Academy of Sciences* **116**, 40 (2019), 1987519879 [14]. Kevin A. Cremin, Jingdi Zhang, Christopher C. Homes, G. D. Gu, Zhiyuan Sun, Michael M. Fogler, Andrew J. Millis, D. N. Basov, and Richard D. Averitt. The thesis auther was the primary author of this chapter.

Funding from Department of Energy Basic Energy Sciences DE-SC0018218 is acknowledged. Work at Brookhaven National Laboratory was supported by the Office of Science, U.S.

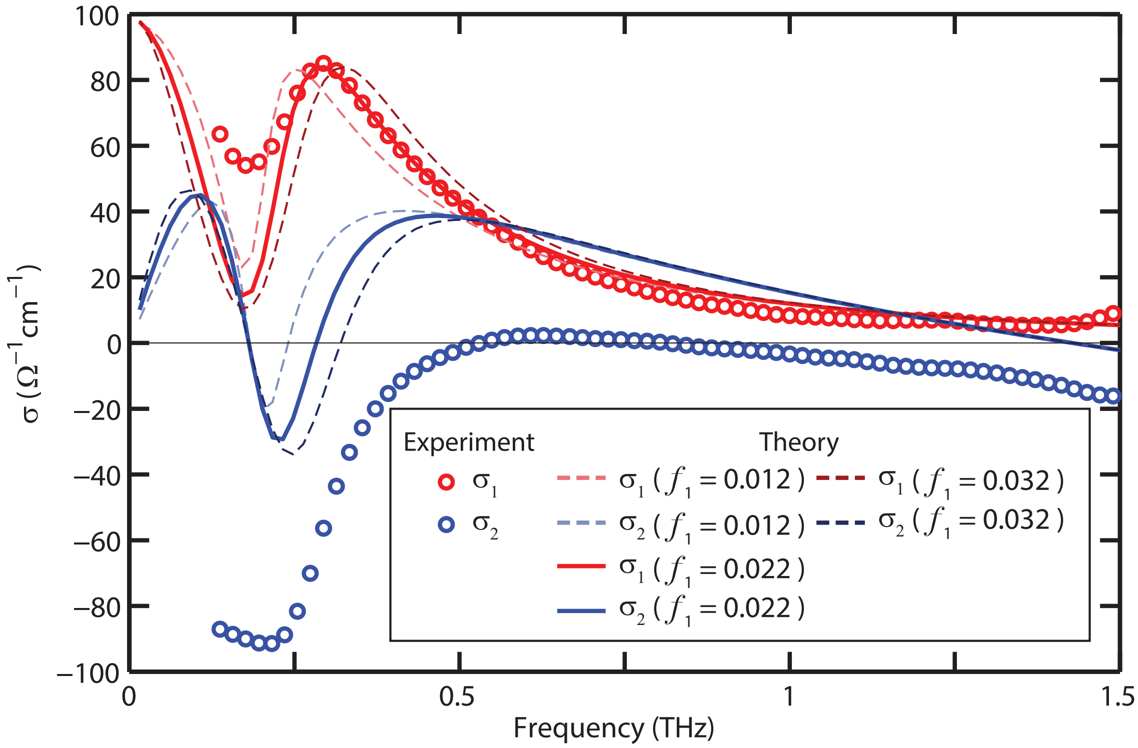

Figure 4.6: Optical conductivity of the photo-excited meta-stable phase in LBCO at 7K. The red and blue dots are experimental data and the solid and dashed lines are the optical conductivity calculated from the effective medium model with varying values of the filling fractions. The model shown in Fig. 4.5(c) is the same as the solid curve plotted here.

Department of Energy under Contract DE-SC0012704. We thank Danielle Nicoletti and Andrea Cavalleri as well as Ryo Shimano and Rysuke Matsunaga for fruitful discussions.

Chapter 5

Nonlinear c-axis measurements in $La_{2-x}Sr_xCuO_4$: Third harmonic generation and Josephson plasma resonance-metamaterial coupling

5.1 Introduction

In recent decades the technological advancements in time-domain spectroscopy have opened up new avenues of studying quantum materials, especially superconductors with low energy excitations [5, **?**]. With the use of low energy THz light, we are able to directly probe the response of quantum materials and observe how they react upon excitation. The advancement of generating intense THz pulses has also created a means to measure pump or probe nonlinearities in materials. The past several years has seen much research utilizing nonlinear THz spectroscopy to observe Higgs mode oscillations in BCS superconductors. Where light couples non-linearly to the Higgs mode of the superconducting condensate and pseudospin prescession with twice the pump frequency[49, 48, 11, 57, **?**, **?**, 13]. One can think of linear measurements only being able to capture a fraction a materials full response.

The development of metasurfaces or metamaterials interacting with matter, typically consisting of arrays of split ring resonators, has also attracted much attention over recent decades and has opened up avenues to study light-matter coupling [**?**, **?**, **?**] and can be fabricated on a wide variety of materials. Metamaterial fabrication has evolved as well, allowing the possibility of printed flexible polyimide tapes which can easily be applied and removed from a materials surface[70]. Jacob Schalch *et. al.* [62] have applied metamaterial tapes to *c*-axis $La_{1.885}Ba_{0.15}CuO_4$ (LSCO) and demonstrate coupling between the Josephson plasma resonance and the metamaterial resonance. In essence, this report is a continued effort to observe strong coupling int LSCO. We utilize the combined effect of intense THz fields and improved metamaterial construction, decreasing the distance from metamaterial to LSCO by a factor of 10. First, a systematic nonlinear THz study of bare LSCO's *c*-axis response is measured using THz time domain spectroscopy techniques discussed in chapter 2. We observe significant third-harmonic generation as a result of the higher order nonlinear effects of the Josephson effect. Then measure the response of the LSCO-metamaterial coupling by applying the newly developed tapes.

5.2 Methods

In this report, we use THz time domain spectroscopy to study the nonlinear response of cuprate superconductors LSCO and LBCO. The intense THz radiation is generated via optical rectification of a near infrared pulse inside a Mg-$LiNbO_3$(LNO) crystal using a tilted pulse front technique which is described in chapter 2. We use 3 mJ pulses from a 1kHz regenerative Ti:sapphire amplifier incident on a LNO crystal to generate THz pulses at the sample position with energies of 2 μJ. The THz output from the LNO crystal surface is then collimated in a PTX lens (f = 120 mm) and focused onto the sample with a parabolic mirror (f=101.6 mm) with an angle of incidence of 15^{o} (s-polarized) and a beamsize of 2.3 mm FWHM. Before reaching the sample, the THz passes through a pair of wire grid polarizers (WGP) which are used to attenuate the THz field intensity down to roughly 2% of the maximum, and this has little affect on the temporal profile and spectrum of the THz as is attenuated. The maximum field strength achieved at the sample is $\sim$ 80 kV/cm with this experimental setup. The reflection off the sample surface is collected and collimated and focused ($f = 54.45$ mm and $f = 50.8$ mm respectively) onto a 300 μm thick (110) GaP crystal for EO sampling. The GaP crystal is mounted on a 2 mm thick (100) GaP cut crystal, which helps push the etalon reflected from the back crystal surface to a later arrival time. The (100) crystal cut does not produce optical rectification for normal incidence but index matches the (110) cut minimizing internal reflection. Roughly 1% of the pump beam is split off and used for gating the THz pulse in the GaP crystal. A detailed schematic of the experimental setup is shown in Fig. 5.1.

The crystals studied were cut and polished to expose the a-c plane and oriented for THz measurements parallel to the c-axis. Both single crystals $La_{1.85}Sr_{0.15}CuO_4$ and $La_{1.885}Ba_{0.115}CuO_4$ were grown via a traveling-solvent floating-zone method[68] and have a surface size roughly 3mm x 3mm and 5mm x 5mm, respectively. The c-axis reflectivity measurements were performed by taking time domain scans of the electric field $E_s(t)$ reflected off the sample and $E_r(t)$ reflected from a gold mirror at the sample position as a reference. The reflectivity is then obtained by calculating $R = |\tilde{E}_s(\omega)/\tilde{E}_r(\omega)|^2$ were $\tilde{E}_s(\omega)$ and $\tilde{E}_r(\omega)$ are the respective Fourier transforms of the time domain scans. Measurements were performed over temperatures above and below T_c and for several field strengths which are presented in section 5.3.

The metamaterials applied to the crystal surface were fabricated onto a sort of flexible polyimide ”tape” which can be easily removed and reapplied to another surface, which allows us to examine different metamaterial designs on the exact same crystal. The ability to do so, eliminates any deviations in sample quality while performing a parameter sweep of metamaterial design. The development and use of metamaterial tapes has been demonstrated successfully as

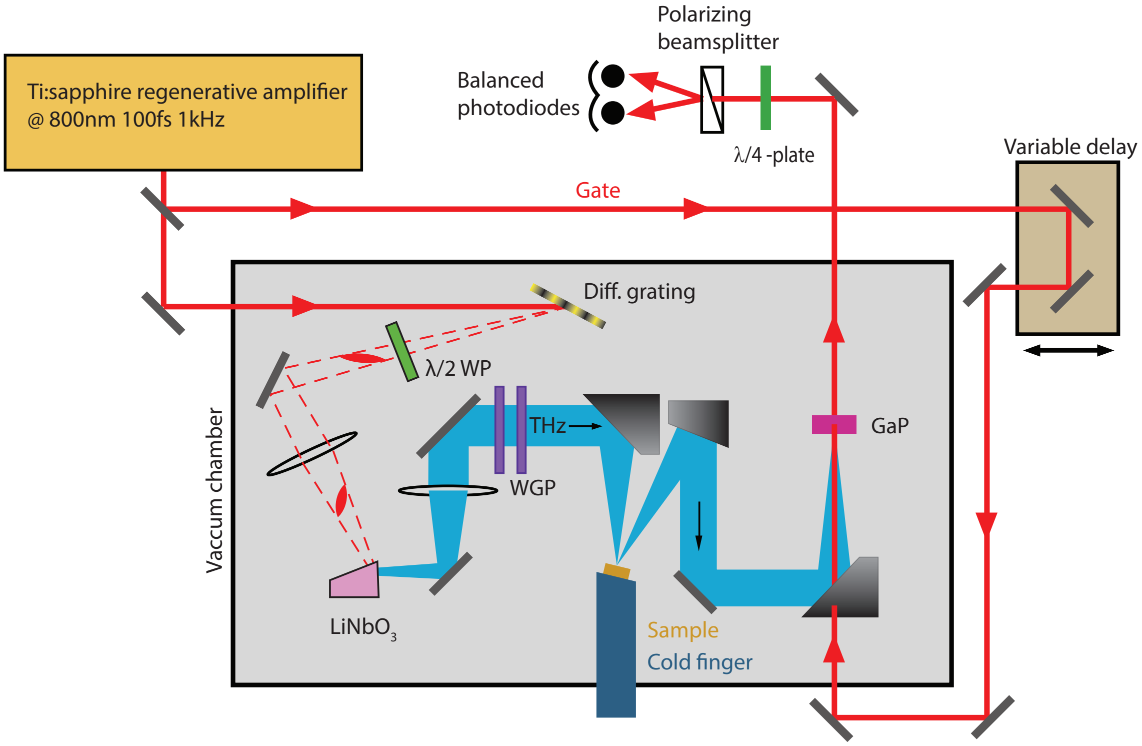

Figure 5.1: Experimental schematic of high field THz time domain spectroscopy setup. The intense THz pusle is generated in a $LiNbO_3$ crystal using a tilted pulse front technique and detected in a GaP crystal.

a THz absorber[70] and coupling to the JPR in LSCO [62]. Recent development in fabricating the tapes has allowed the metamaterial resonator itself to closely space from the sample surface by only 200 nm, opening the door to the strong coupling regime. The fabrication of the flexible structures begins by spin coating an 8 μm thick layer of liquid polyimide onto a silicon wafer to act as a support. The wafer is then placed in a oven and cured for 5 hours at 350^{o} C in an nitrogen atmosphere. An array of split-ring resonators $\sim$200 nm thick is patterned on top of the polyimide surface using direct laser writing. Our goal here is to place the resonator at a very small but finite distance from the superconducting surface as to not short out the gap, so the tape is coated again with another 1 μm layer of polyimide to act as an insulating layer. Spin coating alone offers poor precision in the thickness of the deposited layer, so the top 1 μm coat is etched away leaving the final polyimide surface only 200 nm from the metamaterial layer. The polyimide tapes were adhered to the polished crystal surface by depositing a few drops of methanol and carefully orienting and placing the tapes on top. A clean q-tip was then used to flatten the tape for uniform contact with the surface, and waiting several minutes for the methanol to dry. Once dried, the metamaterial tape was adhered to the crystal surface and could be mounted into the experimental setup. Any surface defect or contamination can affect the uniformity of the tapes distance to the crystal surface which will directly affect the coupling (distance) of the metamaterial to the samples resonances.

The metamaterial structures were designed and simulated using CST-microwave studio software, which uses a finite difference time domain method to solve Maxwell's equations[77, 65] allowing for temporal and frequency resolved response of an initialized material or heterostructure. The metamaterials used in this experiment were designed to have a strong resonance near 0.65 THz when sitting on the superconducting surface of LSCO at 10 K. The resonance is also accompanied by a large field enhancement of $E_{\text{incident}}(\omega)$ within the capacitave gap. The in-gap field enhancement, shown in Fig. 5.2(a), peaks at the metamaterial resonant frequency and reaches a enhancemnet factor of $\sim$ 60 at 0.65 THz which also coincides with the peak intensity

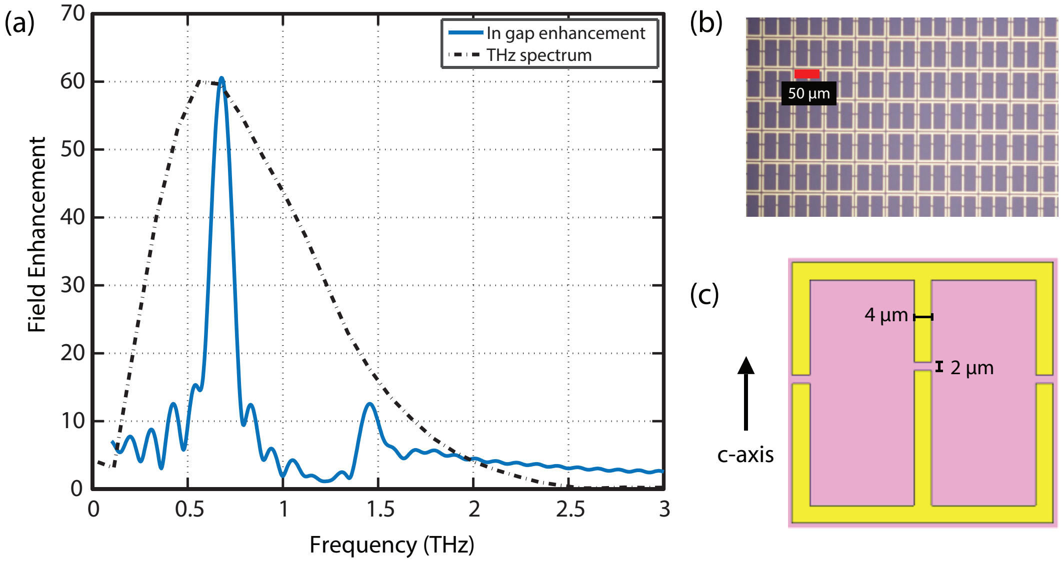

Figure 5.2: (a) THz field enhancement within the metamaterial's capacitive gap as a function of frequency (blue curve) measured just above superconducting LSCO at 10K. The enhancement is calculated in the time domain simulations done in the CST software. The dashed curve is the THz spectrum for comparison. (b) Microscopic image of the actual patterned array of metamaterials on the polyimide tape. (c) Diagram of a unit cell structure with dimensions of the gap.

of the THz pulse plotted as a black dashed line. Figure 5.2(b) and (c) show a microscope image of the patterned array within the polyimide tape and a schematic diagram of the metamaterial unit cell respectively.

5.3 Results

5.3.1 $La_{2-x}Sr_xCuO_4$ *c*-axis reflectivity

We begin by first looking at the the measurements performed on the bare $La_{2-x}Sr_xCuO_4$ crystal. The c-axis THz reflectivity is plotted in Fig. 5.3(a) for several temperatures above and below $T_c = 38$ K, and we can see a clear plasma edge form and sharpen with decreasing temperature from 32 K to 10 K coinciding with an increase in superconducting carriers. The low temperature plasma edge $\omega_p(10\text{ K}) \sim 1.7$ THz is in agreement with previous c-axis measurements of $x = 0.15$ doping [67, 17]. Figure 5.3(b) shows the plasma frequency $\omega_p(T)$ normalized by the low temperature measurement ω_p(10 K) and scales as the typical Ginzburg-Landau behavior for a second order phase transition(dashed line).The inset of Fig. 5.3(b) displays the loss function -Im$(1/\varepsilon)$ at each temperature.

We note that for frequencies below ω_p the reflectivity is $\sim$90% whereas a typical plasma edge approaches unity reflection as $\omega \to 0$. We attribute this deviation to a beamsize issue, where there may slight clipping of the focused THz beam on the sample, which translate to less reflected THz compared to off of the gold reference mirror. This effect is greater for lower frequencies since the focused THz beam diameter d is frequency dependent according to the diffraction limit $d \propto (\lambda f)/D$ where λ is the wavelength of light, f is the focal length, and D is the collimated beam aperture. The reflectivity at 45 K is also slightly decreasing for frequencies $\omega > 1.5$ THz which differs from a rather flat reflectivity curve measured above T_c in previous measurements[67]. This could be a result from imperfections in the surface smoothness, causing the higher frequencies of THz to scatter off the surface slightly more.

When probing the c-axis response with higher electric field strengths the nonlinear material properties become apparent. Figure 5.4 displays the measured c-axis reflectivity of $La_{1.85}Ba_{0.15}CuO_4$ at several field strengths up to 80 kV/cm. There are two main features observed in reflectivity which are changing with increasing field strength: a redshift in the Josephson plasma frequency and increased reflectivity above the plasma edge. These features can be further understood by examining the higher order terms in the phase dynamics phase dynamics of layered superconductors described by the Josephson equations[61, 45].

In a layered superconductor, the interlayer phase difference $\theta(t)$ changes over time according to the second Josephson equation

$$\frac{\partial\theta(t)}{\partial t} = \frac{2edE(t)}{\hbar} \tag{5.1}$$

where $2e$ is the cooper pair charge, d is the interlayer spacing ($\sim$1 nm), $\hbar$ is Planck's constant

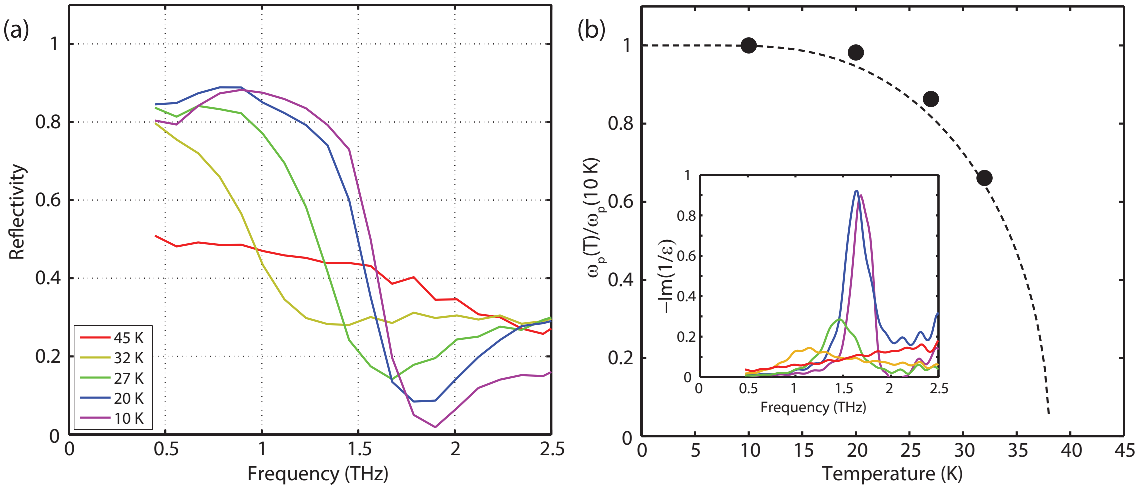

Figure 5.3: (a) Linear c-axis reflectivity of bare $La_{1.85}Ba_{0.15}CuO_4$ at several temperatures.Then linear measurements were taken with the lowest attenuated THz field. (b) C-axis Josephson plasma resonance ω_p plotted for temperatures below T_c, and the dashed line represents the Ginzburg-Landau order parameter scaling for second order phase transitions. The plasma frequencies are normalized to the low temperature measurement $\omega_p(T = 10\text{ K})$. The inset shows the loss function which is the imaginary part of $-1/\varepsilon$, and contains the same colors as the legend in panel (a).

divided by 2π and for an electric field along the c-axis $E(t) = E_0 \sin(\omega_{\text{pump}} t)$ where E_0 is the field strength and oscillates at frequency ω_{pump}. Solving equation 5.1 yields the relation $\theta(t) = (2edE_0/\hbar)\cos(\omega_{\text{pump}} t)$. Since the c-axis superconducting superfluid density ρ_c scales as the order parameter phase difference $\rho_c \propto \cos\theta$ and that $\rho_c \propto \omega_p$ as shown in Fig. 5.3(b), the plasma frequency renormalizes according to $\omega^2_{nonlin} = \omega_p \cos\theta(t)$ where $\omega_{nonilin}$ is the new Josephson plasma frequency under intense field strengths. By inserting $\theta(t)$ and expanding the ω_{nonlin} we arrive at

$$
\begin{aligned}
\omega^2_{JPR1} &= \omega^2_{JPR0}\cos(\theta) = \omega^2_{JPR0}\cos\left[\theta_0 \cos(\omega_{pump} t)\right] \\
&\approx \omega^2_{JPR0}\left[1 - \frac{\theta_0^2}{4} - \frac{\theta_0^2 \cos(2\omega_{pump} t)}{4} + \dots\right]
\end{aligned}
\tag{5.2}
$$

where $\theta_0 = 2edE_0/\hbar$. From this expansion we can see that the next leading order term is

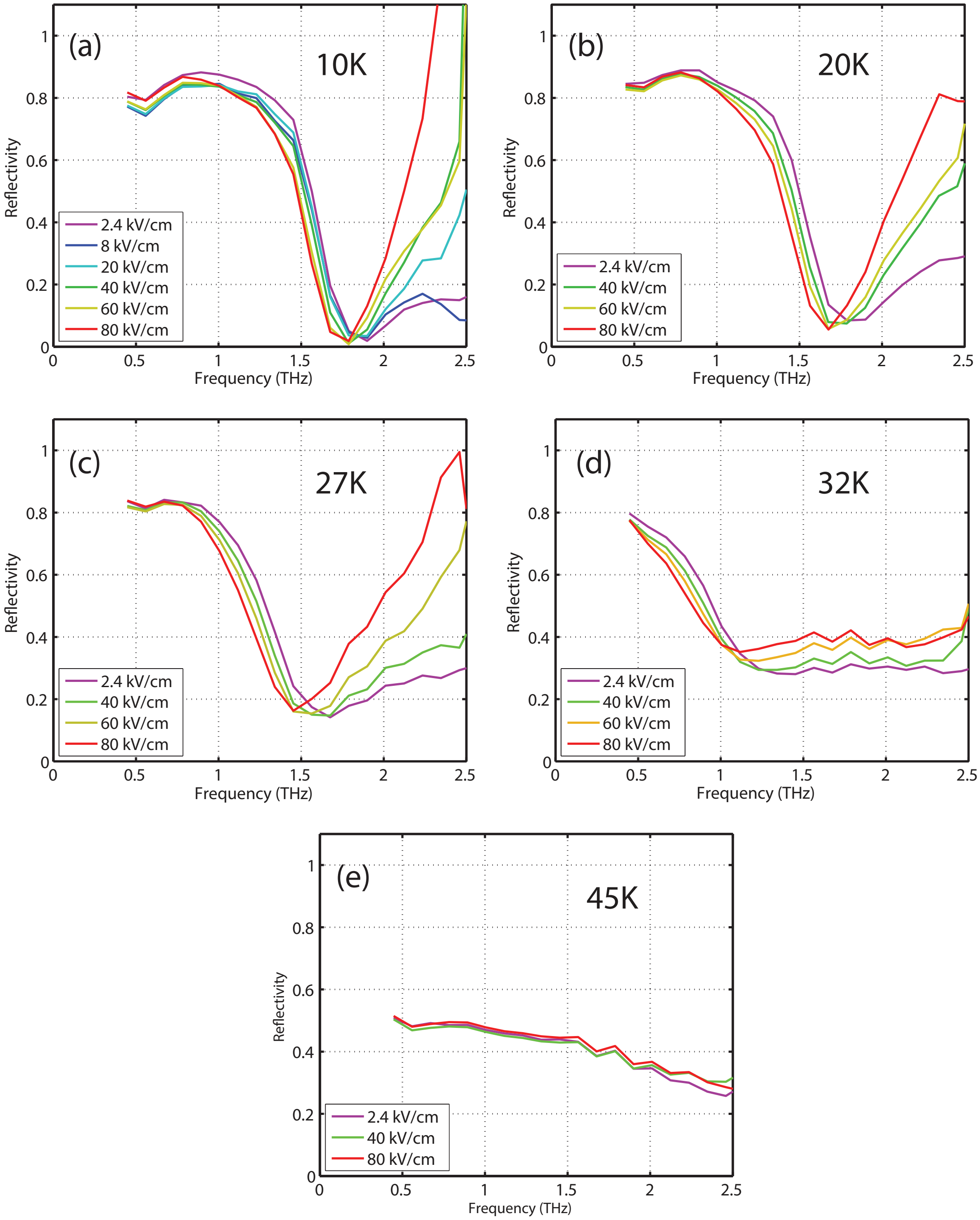

Figure 5.4: c-axis THz reflectivity of $La_{1.85}Sr_{0.15}CuO_4$ at various temperatures and field strengths. Panels (a)-(e) show the reflectivity taken at temperatures 10K, 20K, 27K, 32K, and 45K respectively.

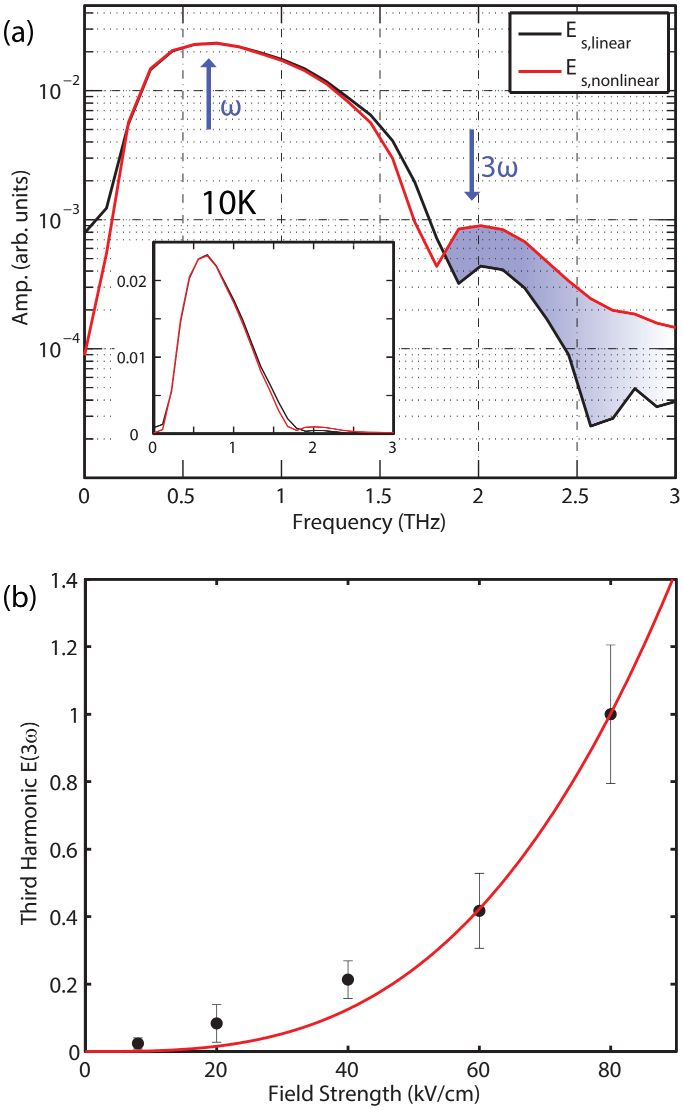

Figure 5.5: Third harmonic generation from *c*-axis LSCO at 10K. (a) Linear (black) and nonlinear (red) spectrum of the THz pulse $E_s(\omega)$ reflected from the sample. The nonlinear spectrum is that from the maximum field strength of ∼80 kV/cm, and the linear spectrum is taken from the minimum field strength renormalized (details explained in the text). The shaded region in blue is the spectral content attributed to third harmonic generation. The inset contains a plot of the two spectrum in a linear vertical scaling. (b) Third harmonic generation at as a function of incident THz field strength at 10K. Each data point is an integrated difference $\int (E_{s,nonlinear} - E_{s,linear}) d\omega$ over the third harmonic region and a cubic polynomial fit is plotted in red.

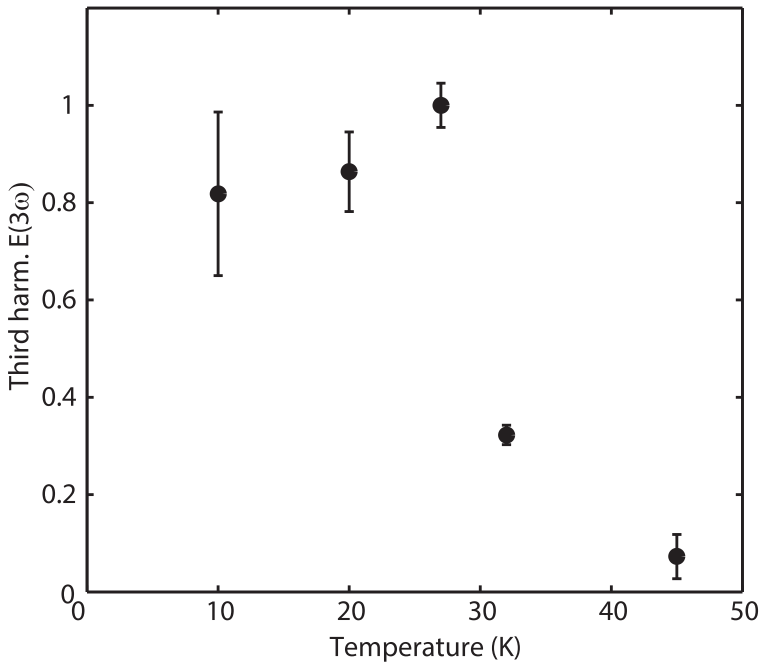

Figure 5.6: Magnitude of c-axis third harmonic emission from LSCO at several temperatures. All data points were taken with maximum field strengths of 80 kV/cm.

subtracting resulting in a redshift in the plasma frequency which is what is observed below T_c for high fields and is shown in Fig. 5.4, which also occurs as temperature increases.

The tunneling interlayer current depends on the phase difference by $I(t) = I_0 \sin[\theta(t)]$, and solving for $I(t)$ gives

$$\begin{aligned} I(t) &= I_c \sin\left[\theta_0 \cos(\omega_{\text{pump}} t)\right] \\ &\approx I_c\left[\theta_0 \cos(\omega_{\text{pump}} t) - \frac{\theta_0^3}{6}\cos^3(\omega_{\text{pump}} t) + \ldots\right] \end{aligned} \tag{5.3}$$

where the leading higher order in the expansion is cubic. This expanded term leads to driving the current at the thrid hamrnonic and is observed as THz emission at 3ω and explains the increase in reflectivity above the plasma edge in Fig. 5.4(a)-(d).

We quantify the amount of third harmonic emission from driving the c-axis by integrating

$$E_{3\omega} = \int \left[|\tilde{E}_{s,nonlin}(\omega)| - |\tilde{E}_{s,lin}(\omega)| \right] d\omega \tag{5.4}$$

where $\tilde{E}_{s,nonlin}(\omega)$ and $\tilde{E}_{s,lin}(\omega)$ are the spectral content reflected from the sample in the nonlinear and linear regime. We take the lowest measured field strength 2.4 kV/cm to be within the linear regime, but in order to compare the two spectra, we rescale the linear spectra with the reflection coefficient at the minimum fluence to obtain $\tilde{E}_{s,lin} = \tilde{E}_{r,nonlin}\tilde{r}_{min}$. Here the reflection coefficient is given by $\tilde{r}_{min} = \dfrac{\tilde{E}_{s,min}}{E_{r,min}}$ where $\tilde{E}_{r,nonlin}$ and $\tilde{E}_{r,min}$ are the spectra of the two reference pulses reflected off a gold surface at the nonlinear and minimum field strengths. The two spectra of $E_{s,nonlin}(\omega)$ and $E_{s,lin}$ for the highest field strength of 80 kV/cm at 10K are plotted in Fig. 5.5(a), and the difference is shaded in blue. To avoid summing over the Josephson plasma edge, the third harmonic integration is taken from 1.8 THz to 2.4 THz. The increase in spectra peaks around 1.9 THz which is the three times the peak of the THz pulse, at 1.65 THz. Figure 5.5(b) displays the magnitude of the third harmonic $E_{3\omega}$ as a function of field strength at 10 K, along with a cubic polynomial fit(red line). We note that the cubic fit resulted with R-squared value of 0.99 where as a quadratic fit resulted in a value 0.96 further indicating that the emission follows the cubic scaling in equation 5.3. The scaling of the third harmonic emission also scales similarly to the superconducting order parameter as demonstrated in Fig.5.5 where the third harmonic magnitude is plotted as a function of temperature. To our knowledge, third harmonic emission from c-axis cuprates has only been previously observed in $La_{2-x}Ba_xCuO_4$[58] and shares similar characteristics as our results. We estimate the third harmonic power conversion efficiency to be $(E_{3\omega}/E_{r,nonlin})^2$ =6x10^{-5} which is comparable to the THz third harmonic generation efficiency from the Higgs mode in BCS superconductor NbN[49, 48].

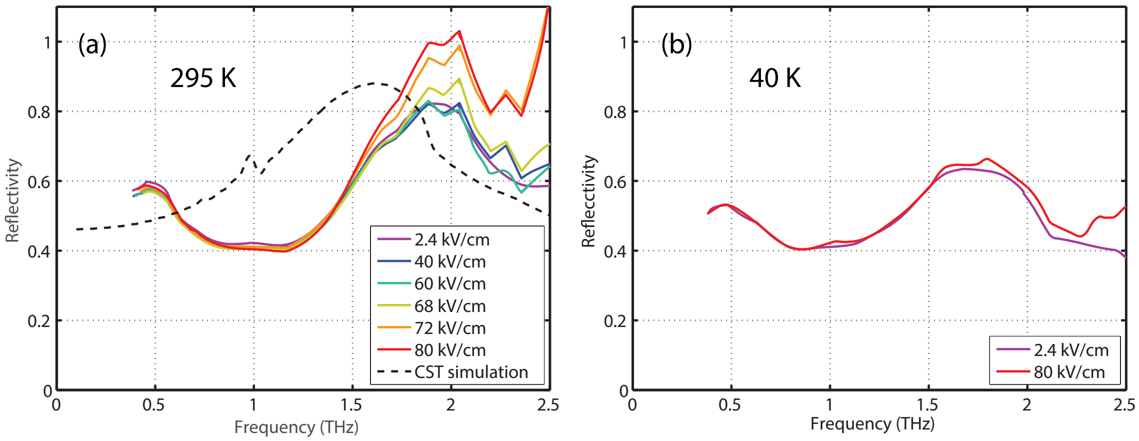

Figure 5.7: C-axis reflectivity of LSCO with asymmetrical metamaterial tape at 295 K (a) and 40 K (b). The capacitive gap of the metamaterial is aligned such that it lies along the c-axis of the crystal. The dashed curve in panel (a) is a CST simulation of the metamaterial on LSCO at 295 K.

5.3.2 $La_{2-x}Sr_xCuO_4$ with asymmetrical metamaterial

We will now discuss the affect of applying the metamaterial tape discussed previously to the surface of LSCO. The metamaterial tape was oriented on the crystal such that the capacitave gap is parallel along the c-axis. Interestingly, we observe nonlinear behaviour in reflectivity above T_c which was not observed on the bare sample. At room temperature, CST simulations show the metamaterial and LSCO together have a broad resonance near 1.5 THz which is displayed as a dashed line in Fig. 5.7. The measured reflectivity displays a resonance peak slightly bueshifted from the simulation which is within reason given that small offsets in the polyimide layer thickness or small vacuum gap between the tape and LSCO surface can directly affect or shift the resonance frequency.

Surprisingly, at room temperature we observe an increase in reflectivity around 2 THz for incident fields above 70 kV/cm. At first look, this appears similar to the third-harmonic generation we have observed in the bare superconducting LSCO. With such a high field enhancement of ~ 60, the in gap THz field intensity may be several MV/cm which is within range to drive nonlinearities in many types of materials. THz high harmonic generation has been observed semiconductors like silicon [55], graphene[28], and array of non-centrosymmetric materials[71]. The response at lower temperatures, but still above T_c is plotted in Fig. 5.7(b) and does not show the same field dependent response at 295 K. The peak of the metamaterial resonance also slightly redshifts, most likely due to a decrease in the *ab*-plane resistivity. Upon further inspection of the data by applying the same analysis to the bare LSCO field dependence we can quantify the increase in spectral content as a function of incident field strength. The increase in spectra around 2 THz is quantified by using equation 5.4 where E_{lin} is obtained from the measurement at a field strength of 2.4 kV/cm. Figure 5.8 shows the integrated spectra versus field strength which displays non-cubic behaviour suggesting not third harmonic generation. The trend appears more like there is a threshold around 70 kV/cm for a change to occur and then increases linearly with field strength, which may be attributed to an increase in the strength of the metamaterial resonance with increasing field strength. Further experiments will be needed to determine the mechanism occurring at room temperature.

We now turn to examine the low temperature *c*-axis response of the metamaterial on superconducting LSCO which is plotted in Fig. 5.9. The first observation is that the Josephoson plasma resonance is greatly redshifted to near 1 THz as appose to $\sim$1.7 THz in the bare sample. The new plasma edge also continues to redshift with increasing fields, indicating that this resonance is truly the Josephson plasma resonance. A low field measurement, using a ZnTe for THz generation, is plotted in grey and shows similar behavior with a redshifted plasma edge but differs at higher frequencies. Figure 5.9(b) shows the simulation of the metamaterial on LSCO at 10 K which displays a much weaker redshift of the plasma edge only to 1.5 THz. The two sharp *LC* resonances at 0.5 THz and 0.6 THz are not observed in our measurements and are likely at lower frequencies outside of our spectral range.

Comparing the low field response and the nonlinear response leaves more questions to be answered. If the increased spectral content above 1.5 THz is from third-harmonic generation, as we observe in bare LSCO, then the field strength may be in a saturated regime and unable to

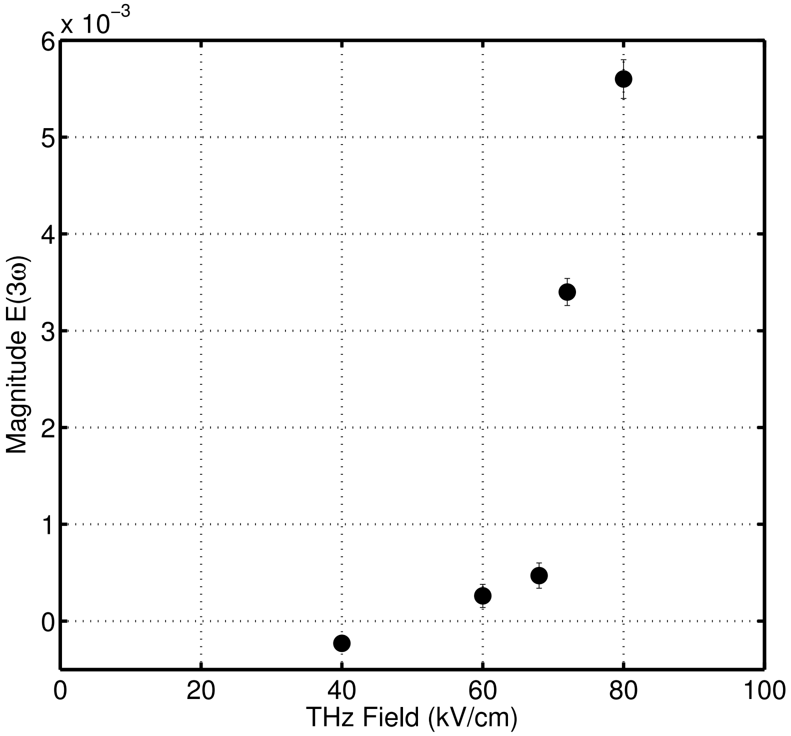

Figure 5.8: Increase in c-axis spectral weight, reflected from the metamaterial on LSCO, versus incident field strength at 295 K. Each data point is the integrated spectra $\int(E_{nonlin} - E_{lin})d\omega$ over the frequency range 1.5 THz - 2.4 THz.

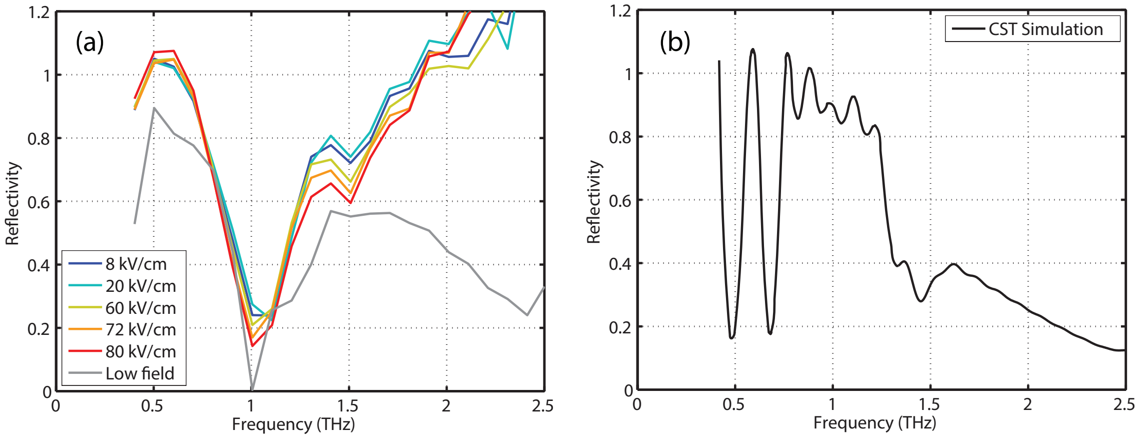

Figure 5.9: C-axis reflectivity of LSCO with asymmetrical matamaterial tape below T_c at 10K.(a) Reflectivity measured for several THz field strengths(colored lines), and low field measurement (grey line) at 10 K performed using ZnTe as a THz generation source for comparison. (b) Reflectivity from CST simulation of the metamaterial tape on superconducting LSCO.

observe a field dependent scaling. The enhanced strength of the THz field should be strong enough to be within the strong-coupling regime of the *LC* resonance and Josephon plasma resonance, but more measurements and metamaterial variations will be needed to conclude beyond speculation the type of coupling that we are observing here.

5.4 Conclusion

We have explored the nonlinear *c*-axis response of *LSCO* and have made the first observations of THz third-harmonic generation from the Josephon plasma resonance in this material. The emission from the sample under intense THz radiation displays cubic behaviour indicative of third harmonic generation. By using the strong field enhancement we have been able to probe the materials nonlinearities even further above and below T_c. More experimentation will be needed to address the extent which strong-coupling is occurring.

5.5 Acknowledgements

This work is unpublished and shows our preliminary results. Kevin Cremin, Kelson Kaj, Ian Hammock, Jacob Schalch, Chunxu Chen, Xiaguan Zhao, Dimitri Basov, Xin Zhang, Richard Averitt. The thesis author was the author of this chapter.

Appendix A

Pump induced heating in LBCO

Heating effects are present in all pump probe measurements and the effective lattice temperature must be considered after photo-excitation. We use a two-temperature model to estimate the final lattice temperature after electron-phonon thermalization has occurred (in ∼1 ps)[1]. The specific heat for $La_{2-x}Ba_xCuO_4$ is described by the relation

$$C_s = \gamma T + \beta T^3 \tag{A.1}$$

over a wide temperature range[53], where γ and β are the electronic and lattice coefficients to the specific heat, respectively. Specific heat coefficients were taken as $\gamma \sim 2.5$ mJ mol^{-1} K^{-2} and $\beta \sim 0.25$ mJ mol^{-1} K^{-4} estimated from literature values of nearby dopings5. For a given pump fluence we estimate the absorbed energy over the photo-excited region and calculate the effective temperature after electron-phonon thermalization by integrating

$$Q_{pump} = \int_{T_i}^{T_f} NC_s(T)dT, \tag{A.2}$$

where Q_{pump} is the total energy absorbed from the pump pulse, N is the number of moles in the excited volume, T_i is the initial temperature and T_f is the final temperature after electron-phonon

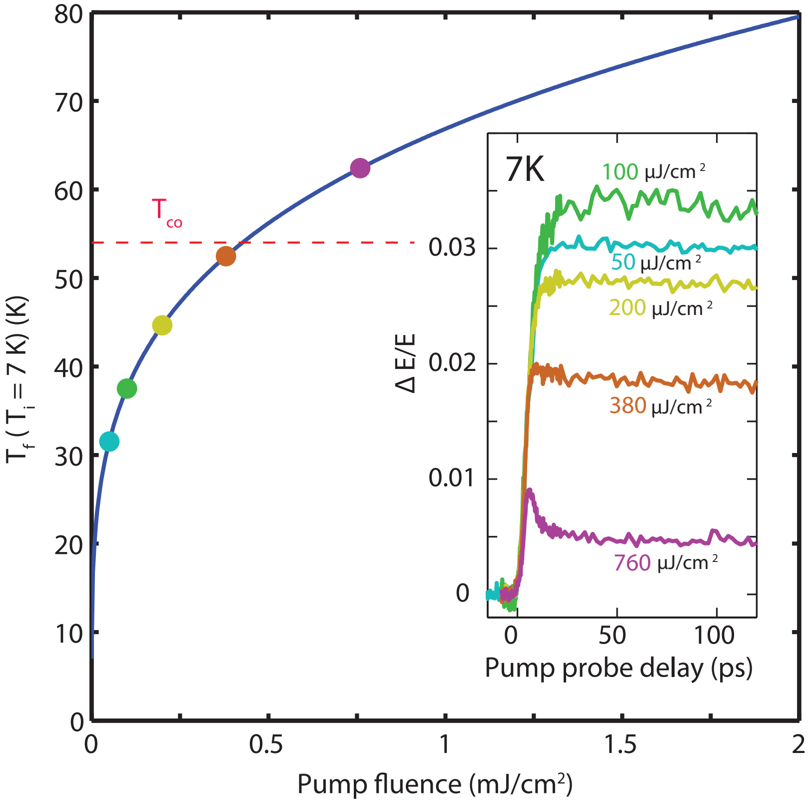

Figure A.1: Calculated final lattice temperature after electron-phonon thermalization in LBCO. The colored dots represent T_f for a given fluence which are color coordinated with the inset figure. The inset is the time dependent relative change in the THz electric field amplitude after excitation at various pump fluences (at 7 K). The red dashed line is the charge order transition temperature T_{co}.

thermalization. The absorbed energy Q_{pump} is estimated by $Q_{pump} = FA(1-R)$ where F is the pump fluence, A is the area of the pump beam on the sample using the FWHM (∼6 mm) as the diameter, and R is the reflectivity at 1.55 eV which is ~ 0.151. The excited volume is estimated as a cylindrical disk with a diameter of 6 mm and height equal to the penetration depth.

The final temperature T_f is calculated numerically and plotted versus pump fluence in Fig. A.1 for an initial temperature T_i = 7 K. The colored points correspond to the various fluences used in the experiment and the $\Delta E/E$ pump probe traces displayed in the inset.

Bibliography

[1] Allen, P. B. Theory of thermal relaxation of electrons in metals. *Physical Review Letters 59*, 13 (1987), 1460–1463.

[2] Aslamazov, L. G., and Larkin, A. I. The Influence of Fluctuation Pairing of Electrons on the Conductivity of Normal Metal. *Physics Letters 26*, 6 (1968), 238–239.

[3] Auston, D. H., Cheung, K. P., Valdmanis, J. A., and Kleinman, D. A. Cherenkov radiation from femtosecond optical pulses in electro-optic media. *Physical Review Letters 53*, 16 (1984), 1555–1558.

[4] Barbara, P., Cawthorne, A. B., Shitov, S. V., and Lobb, C. J. Stimulated emission and amplification in josephson junction arrays. *Physical Review Letters 82*, 9 (1999), 1963–1966.

[5] Basov, D., and Timusk, T. Electrodynamics of high-Tc superconductors. *Rev. Mod. Phys. 77*, April (2005), 721–779.

[6] Bednorz, J., and Müller, K. Possible high T c superconductivity in the BaLaCuO system Springer Netherlands, 1986. 267-271. 5.

[7] Blanchard, F., Razzari, L., Bandulet, H., Sharma, G., Morandotti, R., Kieffer, J. C., Ozaki, T., Reid, M., Tiedje, H. F., Haugen, H. K., and Hegmann, F. A. Generation of 1.5 J single-cycle terahertz pulses by optical rectification from a large aperture ZnTe crystal. *Optics Express 15*, 20 (2007), 13212.

[8] Blanchard, F., Ropagnol, X., Hafez, H., Razavipour, H., Bolduc, M., Morandotti, R., Ozaki, T., and Cooke, D. G. Effect of extreme pump pulse reshaping on intense terahertz emission in lithium niobate at multimilliJoule pump energies. *Optics Letters 39*, 15 (2014), 4333.

[9] Borodianskyi, E. A., and Krasnov, V. M. Josephson emission with frequency span 1-11 THz from small Bi2Sr2CaCu2O8+δ mesa structures. *Nature Communications 8*, 1 (2017), 1–6.

[10] Casandruc, E., Nicoletti, D., Rajasekaran, S., Laplace, Y., Khanna, V., Gu, G. D., Hill, J. P., and Cavalleri, A. Wavelength-dependent optical enhancement of superconducting interlayer coupling in L a1.885 B a0.115Cu O4. *Physical Review B - Condensed Matter and Materials Physics 91*, 17 (2015), 1–7.

[11] Cea, T., Castellani, C., and Benfatto, L. Nonlinear optical effects and third-harmonic generation in superconductors : Cooper pairs versus Higgs mode contribution. 1–5.

[12] Chang, J., Blackburn, E., Holmes, A. T., Christensen, N. B., Larsen, J., Mesot, J., Liang, R., Bonn, D. A., Hardy, W. N., Watenphul, A., Zimmermann, M. v., Forgan, E. M., and Hayden, S. M. Direct observation of competition between superconductivity and charge density wave order in $YBa_2Cu_3O_{6.67}$. *Nature Physics 8*, 12 (dec 2012), 871–876.

[13] Chu, H., Kim, M.-j., Katsumi, K., Kovalev, S., Dawson, R. D., Yoshikawa, N., Kim, G., Putzky, D., Li, Z. Z., Germanskiy, S., Deinert, J.-c., Awari, N., Ilyakov, I., Green, B., Chen, M., Bawatna, M., Christiani, G., Logvenov, G., Gallais, Y., Boris, A. V., Keimer, B., Schnyder, A., Manske, D., Gensch, M., Wang, Z., Shimano, R., and Kaiser, S. New collective mode in superconducting cuprates uncovered by Higgs spectroscopy. 1–28.

[14] Cremin, K. A., Zhang, J., Homes, C. C., Gu, G. D., Sun, Z., Fogler, M. M., Millis, A. J., Basov, D. N., and Averitt, R. D. Photoenhanced metastable c-axis electrodynamics in stripe-ordered cuprate $La_{1.885}Ba_{0.115}CuO_4$. *Proceedings of the National Academy of Sciences of the United States of America 116*, 40 (2019), 19875–19879.

[15] Croft, T. P., Lester, C., Senn, M. S., Bombardi, A., and Hayden, S. M. Charge density wave fluctuations in $La_{2-x}Sr_xCuO_4$ and their competition with superconductivity. 1–8.

[16] Darrow, J. T., Zhang, X. C., Auston, D. H., and Morse, J. D. Saturation Properties of Large-Aperture Photoconducting Antennas. *IEEE Journal of Quantum Electronics 28*, 6 (1992), 1607–1616.

[17] Dordevic, S. V., Komiya, S., Ando, Y., and Basov, D. N. Josephson Plasmon and Inhomogeneous Superconducting State in La 2-xSrxCuO4. *Physical Review Letters 91*, 16 (2003), 1674011–1674014.

[18] Dressel, M., and Gruner, G. *Electrodynamics of Solids.* Cambridge University Press, Cambridge, 2002.

[19] Dreyhaupt, A., Winnerl, S., Dekorsy, T., and Helm, M. High-intensity terahertz radiation from a microstructured large-area photoconductor. *Applied Physics Letters 86*, 12 (2005), 1–3.

[20] FATTINGER, C., AND GRISCHKOWSKY, D. Point source terahertz optics. *Applied Physics Letters 53*, 16 (1988), 1480–1482.

[21] FAUSTI, D., TOBEY, R. I., DEAN, N., KAISER, S., DIENST, A., HOFFMANN, M. C., PYON, S., TAKAYAMA, T., TAKAGI, H., AND CAVALLERI, A. Light-Induced Superconductivity in a Stripe-Ordered Cuprate. *Science 331*, January (2011), 189–192.

[22] FERRINI, G., EISAKI, H., GREVEN, M., DAMASCELLI, A., MAREL, D. V. D., AND PARMIGIANI, F. Disentangling the Electronic and Phononic Glue in a High-Tc Superconductor. *Science 335*, 30 March (2011), 1600.

[23] FEYNMAN, R., LEIGHTON, R., AND SANDS, M. *The Feynman Lectures on Physics, Vol III, Quantum Mechanics*. Addison-Wesley Publishing Company, Inc., 1965.

[24] FUJITA, M., GOKA, H., YAMADA, K., AND MATSUDA, M. Competition between Charge- and Spin-Density-Wave Order in LBCO. *Physical Review Letters 88*, 16 (2002).

[25] FÜLÖP, J. A., PÁLFALVI, L., KLINGEBIEL, S., ALMÁSI, G., KRAUSZ, F., KARSCH, S., AND HEBLING, J. Generation of sub-mJ terahertz pulses by optical rectification. *Optics Letters 37*, 4 (2012), 557.

[26] GIANNETTI, C., CAPONE, M., FAUSTI, D., FABRIZIO, M., PARMIGIANI, F., AND MIHAILOVIC, D. Ultrafast optical spectroscopy of strongly correlated materials and high-temperature superconductors: a non-equilibrium approach. *Advances in Physics 65*, 2 (2016), 58–238.

[27] GRISCHKOWSKY, D., KEIDING, S., VAN EXTER, M., AND FATTINGER, C. Far-infrared time-domain spectroscopy with terahertz beams of dielectrics and semiconductors. *Journal of the Optical Society of America B 7*, 10 (1990), 2006.

[28] HAFEZ, H. A., CHAI, X., IBRAHIM, A., MONDAL, S., FÉRACHOU, D., ROPAGNOL, X., AND OZAKI, T. Intense terahertz radiation and their applications. *Journal of Optics (United Kingdom) 18*, 9 (2016).

[29] HEBLING, J., STEPANOV, A. G., ALMÁSI, G., BARTAL, B., AND KUHL, J. Tunable THz pulse generation by optical rectification of ultrashort laser pulses with tilted pulse fronts. *Applied Physics B: Lasers and Optics 78*, 5 (2004), 593–599.

[30] HIRORI, H., DOI, A., BLANCHARD, F., AND TANAKA, K. Single-cycle terahertz pulses with amplitudes exceeding 1 MV/cm generated by optical rectification in $LiNbO_3$. *Applied Physics Letters 98*, 9 (2011).

[31] HIRORI, H., AND TANAKA, K. Nonlinear optical phenomena induced by intense single-cycle terahertz pulses. *IEEE Journal on Selected Topics in Quantum Electronics 19*, 1 (2013), 8401110.

[32] HOMES, C. C., DORDEVIC, S. V., STRONGIN, M., BONN, D. A., AND LIANG, R. A universal scaling relation in high- temperature superconductors. *Nature 430*, 29 July (2004), 539–541.

[33] HOMES, C. C., HÜCKER, M., LI, Q., XU, Z. J., WEN, J. S., GU, G. D., AND TRANQUADA, J. M. Determination of the optical properties of $La_{2-x}Ba_xCuO_4$ for several dopings, including the anomalous $x = \frac{1}{8}$ phase. *Physical Review B 85*, 13 (apr 2012), 134510.

[34] HU, W., KAISER, S., NICOLETTI, D., HUNT, C. R., GIERZ, I., HOOMANN, M. C., LE TACON, M., LOEW, T., KEIMER, B., AND CAVALLERI, A. Optically enhanced coherent transport in $YBa_2Cu_3O_{6.5}$ by ultrafast redistribution of interlayer coupling. *Nature Mat. 13*, July (2014), 705.

[35] HÜCKER, M., V. ZIMMERMANN, M., GU, G. D., XU, Z. J., WEN, J. S., XU, G., KANG, H. J., ZHELUDEV, A., AND TRANQUADA, J. M. Stripe order in superconducting La¡sub¿2-x¡/sub¿Ba¡sub¿x¡/sub¿CuO¡sub¿4¡/sub¿ 0.095¡x¡0.155. *Physical Review B 83*, 10 (2011), 104506.

[36] JACKSON, J. D. Classical Electrodynamics Third Edition. *American Journal of Physics 67* (1999), 808.

[37] JIE, Q., HAN, S. J., DIMITROV, I., TRANQUADA, J. M., AND LI, Q. Transport properties of stripe-ordered high T_c cuprates. *Physica C: Superconductivity and its Applications 481* (2012), 46–54.

[38] JOSEPHSON, B. D. Possible new effects in superconductive tunnelling. *Physics Letters 1*, 7 (1962), 251–253.

[39] KAKESHITA, T., UCHIDA, S., KOJIMA, K. M., ADACHI, S., TAJIMA, S., GORSHUNOV, B., AND DRESSEL, M. Transverse Josephson plasma mode in T* cuprate superconductors. *Physical Review Letters 86*, 18 (2001), 4140–4143.

[40] KAKEYA, I., AND WANG, H. Terahertz-wave emission from Bi2212 intrinsic Josephson junctions: A review on recent progress. *Superconductor Science and Technology 29*, 7 (2016).

[41] KHANNA, V., MANKOWSKY, R., PETRICH, M., BROMBERGER, H., CAVILL, S. A., MÖHR-VOROBEVA, E., NICOLETTI, D., LAPLACE, Y., GU, G. D., HILL, J. P., FÖRST, M., CAVALLERI, A., AND DHESI, S. S. Restoring interlayer Josephson coupling in La1.885Ba0.115CuO4 by charge transfer melting of stripe order. *Physical Review B 93*, 22 (2016), 1–5.

[42] KUMAGAI, K., MATOBA, H., WADA, N., OKAJI, M., AND NARA, K. Some Anomalies Due to the Low-Temperature Structural Transition around x=0.12 in La¡sub¿2-x¡/sub¿Ba¡sub¿x¡/sub¿CuO¡sub¿4¡/sub¿. *J. Phys. Soc. Jpn. 60*, 5 (1991), 1448–1451.

[43] KUSAR, P., KABANOV, V. V., DEMSAR, J., MERTELJ, T., SUGAI, S., AND MIHAILOVIC, D. Controlled vaporization of the superconducting condensate in cuprate superconductors by femtosecond photoexcitation. *Physical Review Letters 101*, 22 (2008), 1–4.

[44] KUŠAR, P., KABANOV, V. V., SUGAI, S., DEMŠAR, J., MERTELJ, T., AND MIHAILOVIĆ, D. Dynamical structural instabilities in $La_{1.9}Sr_{0.1}CuO_4$ under intense laser photoexcitation. *Journal of Superconductivity and Novel Magnetism 24*, 1-2 (2011), 421–425.

[45] LAPLACE, Y., AND CAVALLERI, A. Josephson plasmonics in layered superconductors. *Advances in Physics: X 1*, 3 (2016), 387–411.

[46] LEE, P. A., NAGAOSA, N., AND WEN, X. G. Doping a Mott insulator: Physics of high-temperature superconductivity. *Reviews of Modern Physics 78*, 1 (2006).

[47] LI, Q., HÜCKER, M., GU, G. D., TSVELIK, A. M., AND TRANQUADA, J. M. Two-dimensional superconducting fluctuations in stripe-ordered $La_{1.875}Ba_{0.125}CuO_4$. *Physical Review Letters 99*, 6 (2007), 4–7.

[48] MATSUNAGA, R., AND SHIMANO, R. Nonlinear terahertz spectroscopy of Higgs mode in s-wave superconductors. *Physica Scripta 92*, 2 (2017).

[49] MATSUNAGA, R., TSUJI, N., FUJITA, H., SUGIOKA, A., MAKISE, K., UZAWA, Y., TERAI, H., WANG, Z., AOKI, H., AND SHIMANO, R. Light-induced collective pseudospin precession resonating with Higgs mode in a superconductor. *Science 345*, 6201 (2014), 1145–1149.

[50] MILTON, G. W. *The Theory of Composites*. Cambridge University Press, Cambridge, 2002.

[51] MITRANO, M., LEE, S., HUSAIN, A. A., DELACRETAZ, L., ZHU, M., DE LA PEÑA MUNOZ, G., SUN, S. X., JOE, Y. I., REID, A. H., WANDEL, S. F., COSLOVICH, G., SCHLOTTER, W., VAN DRIEL, T., SCHNEELOCH, J., GU, G. D., HARTNOLL, S., GOLDENFELD, N., AND ABBAMONTE, P. Ultrafast time-resolved x-ray scattering reveals diffusive charge order dynamics in La2-xBaxCuO4. *Science Advances 5*, 8 (2019).

[52] NICOLETTI, D., CASANDRUC, E., LAPLACE, Y., KHANNA, V., HUNT, C. R., KAISER, S., DHESI, S. S., GU, G. D., HILL, J. P., AND CAVALLERI, A. Optically induced superconductivity in striped $La_{2-x}Ba_xCuO_4$ by polarization-selective excitation in the near infrared. *Physical Review B 90*, 10 (2014), 1–6.

[53] OKAJIMA, Y., YAMAYA, K., YAMADA, N., ODA, M., AND IDO, M. Reduction of the electronic coefficient of the specific heat around x=0.065 in $(La_{1-x}Ba_2)_2CuO_4$. *Solid State Communications 74*, 8 (may 1990), 767–771.

[54] OKAMOTO, J. I., HU, W., CAVALLERI, A., AND MATHEY, L. Transiently enhanced interlayer tunneling in optically driven high-T_c superconductors. *Physical Review B 96*, 14 (2017), 1–7.

[55] Ovchinnikov, A. V., Chefonov, O. V., Mishina, E. D., and Agranat, M. B. Second harmonic generation in the bulk of silicon induced by an electric field of a high power terahertz pulse. *Scientific Reports 9*, 1 (2019), 1–7.

[56] Ozyuzer, L., Koshelev, A. E., Kurter, C., Gopalsami, N., Li, Q., Tachiki, M., Kadowaki, K., Yamamoto, T., Minami, H., Yamaguchi, H., Tachiki, T., Gray, K. E., Kwok, W. K., and Welp, U. Emission of coherent THz radiation from superconductors. *Science 318*, 5854 (2007), 1291–1293.

[57] Pekker, D., and Varma, C. Amplitude/Higgs Modes in Condensed Matter Physics. *Annual Review of Condensed Matter Physics 6*, 1 (2015), 269–297.

[58] Rajasekaran, S., Okamoto, J., Mathey, L., Fechner, M., Thampy, V., Gu, G. D., and Cavalleri, A. Probing optically silent superfluid stripes in cuprates. *Science 359*, 6375 (2018), 575–579.

[59] Ravi, K., Huang, W. R., Carbajo, S., Nanni, E. A., Schimpf, D. N., Ippen, E. P., and Kärtner, F. X. Theory of terahertz generation by optical rectification using tilted-pulse-fronts. *Optics Express 23*, 4 (2015), 5253.

[60] Redi, M. H. Two-dimensional fluctuation-induced conductivity above the critical temperature. *Physical Review B 16*, 5 (1977), 2027–2031.

[61] Savel'Ev, S., Yampol'Skii, V. A., Rakhmanov, A. L., and Nori, F. Terahertz Josephson plasma waves in layered superconductors: Spectrum, generation, nonlinear and quantum phenomena. *Reports on Progress in Physics 73*, 2 (2010).

[62] Schalch, J. S., Post, K., Duan, G., Zhao, X., Kim, Y. D., Hone, J., Fogler, M. M., Zhang, X., Basov, D. N., and Averitt, R. D. Strong MetasurfaceJosephson Plasma Resonance Coupling in Superconducting $La_{2x}Sr_xCuO_4$. *Advanced Optical Materials 7*, 21 (2019), 1–8.

[63] Shibata, H., and Yamada, T. Double Josephson Plasma Resonance in T* Phase $SmLa_{1-x}Sr_xCuO_{4-\delta}$. *Physical Review Letters 81*, 16 (1998), 3519–3522.

[64] Shimano, R., Watanabe, S., and Matsunaga, R. Intense terahertz pulse-induced nonlinear responses in carbon nanotubes. *Journal of Infrared, Millimeter, and Terahertz Waves 33*, 8 (2012), 861–869.

[65] Taflove, A. Application of the FDTD Method to Sinusoidal Steady-State EM Problems, 1980.

[66] Tajima, S., Noda, T., Eisaki, H., and Uchida, S. c -Axis Optical Response in the Static Stripe Ordered Phase of the Cuprates. *Physical Review Letters 86*, 3 (jan 2001), 500–503.

[67] TAMASAKU, K., NAKAMURA, Y., AND UCHIDA, S. Charge Dynamics across the Cu02 Planes in $La_{2-x}Sr_xCuO_4$. *Physical Review Letters 69*, 9 (1992), 1455–1458.

[68] TANAKA, I., YAMANE, K., AND KOJIMA, H. Single crystal growth of superconducting La2-xSrxCuO4 by the TSFZ method. *Journal of Crystal Growth 96*, 3 (1989), 711–715.

[69] TANI, M., MATSUURA, S., SAKAI, K., AND NAKASHIMA, S.-I. Emission characteristics of photoconductive antennas based on low-temperature-grown GaAs and semi-insulating GaAs. *Applied Optics 36*, 30 (1997), 7853.

[70] TAO, H., BINGHAM, C. M., STRIKWERDA, A. C., PILON, D., SHREKENHAMER, D., LANDY, N. I., FAN, K., ZHANG, X., PADILLA, W. J., AND AVERITT, R. D. Highly flexible wide angle of incidence terahertz metamaterial absorber: Design, fabrication, and characterization. *Physical Review B - Condensed Matter and Materials Physics 78*, 24 (2008), 2–5.

[71] TOKURA, Y., AND NAGAOSA, N. Nonreciprocal responses from non-centrosymmetric quantum materials. *Nature Communications 9*, 1 (2018).

[72] TRANQUADA, J. M., GU, G. D., HÜCKER, M., JIE, Q., KANG, H. J., KLINGELER, R., LI, Q., TRISTAN, N., WEN, J. S., XU, G. Y., XU, Z. J., ZHOU, J., AND V. ZIMMERMANN, M. Evidence for unusual superconducting correlations coexisting with stripe order in $La_{1.875}Ba_{0.125}CuO_4$. *Physical Review B 78*, 17 (2008), 1–13.

[73] TRANQUADA, J. M., STERNLIEB, B. J., AXE, J. D., NAKAMURA, Y., AND UCHIDA, S. Evidence for stripe correlations of spins and holes in copper oxide superconductors, 1995.

[74] VAN DER MAREL, D., AND TSVETKOV, A. Transverse optical plasmons in layered superconductors. *Czechoslovak Journal of Physics 46*, SUPPL. 6 (1996), 3165–3168.

[75] VAN DER MAREL, D., AND TSVETKOV, A. A. Transverse-optical Josephson plasmons: Equations of motion. *Physical Review B 64*, 2 (2001), 1–7.

[76] WILKE, I., AND SENGUPTA, S. Nonlinear Optical Techniques for Terahertz Pulse Generation and Detection-Optical Rectification and Electrooptic Sampling. In *Terahertz Spectroscopy: Principles and Applications*, vol. 1. CRC Press, 2007, ch. 2, pp. 41–72.

[77] YEE, K. S. Numerical Solution of Initial Boundry Value Problems INvolving Maxwell's Equations in Isotropic Media. *IEEE Transactions on antennas and propigation* (1966), 169–200.

[78] YU, G., LEE, C. H., HEEGER, A. J., CHEONG, S. W., AND FISK, Z. Photo-excitation of single crystals of $La_2CuO_{4+\delta}$ near the metal-insulator transition. *Physica C: Superconductivity and its applications 190*, 4 (1992), 563–568.

[79] ZHANG, J., AND AVERITT, R. Dynamics and Control in Complex Transition Metal Oxides. *Annual Review of Materials Research 44*, 1 (2014), 19–43.

[80] Zhang, S. J., Wang, Z. X., Shi, L. Y., Lin, T., Zhang, M. Y., Gu, G. D., Dong, T., and Wang, N. L. Light-induced new collective modes in the superconductor $La_{1.905}Ba_{0.095}CuO_4$. *Physical Review B 98*, 2 (jul 2018), 020506.